ISPRS Journal of Photogrammetry and Remote Sensing 183 (2022) 286–306

Contents lists available at ScienceDirect

ISPRS Journal of Photogrammetry and Remote Sensing

journal homepage: www.elsevier.com/locate/isprsjprs

Influence of atmospheric modeling on spectral target detection through forward modeling approach in multi-platform remote sensing data

Sudhanshu Shekhar Jha [a,*], Rama Rao Nidamanuri [a], Emmett J. Ientilucci [b]

[a] Department of Earth and Space Sciences, Indian Institute of Space Science and Technology, Valiamala, Thiruvananthapuram, Kerala, India
[b] Chester F. Carlson Center for Imaging Science, Rochester Institute of Technology, Rochester, NY, USA

ARTICLE INFO

Keywords:
Target detection
Radiative transfer
Aerosol optical thickness
Atmospheric profiles
Aerosol models
Multi-platform dataset

ABSTRACT

Identifying objects or pixels of interest that are few in numbers and sparsely populated in imagery is referred to as target detection. Traditionally, the inverse modeling (IM) approach, usually a slow and computationally intensive process, is used for detecting targets using surface reflectance spectra. For the emerging online methods in remote sensing, modeling the at-sensor radiance of target material, i.e., a forward modeling (FM) approach, can be used. Compared to the IM approach, FM is better suited to online methods due to its potential for adaptation to regional atmospheric modeling. Spectral knowledge transfer of a target from a known to an unknown atmospheric condition is the primary outcome of an efficient target detection framework. However, such an endeavor requires an exhaustive assessment of the target detection process under different atmospheric models and associated uncertainties. The objective of this work is to assess the quantitative impact of atmospheric parameters on the detectability of engineered targets. Specifically, the impact of critical atmospheric parameters such as aerosol optical thickness (AOT), standard atmospheric profiles, and aerosol models are considered. For this effect, we designed a multi-platform image acquisition setup that acquired targets concurrently using a ground-based terrestrial hyperspectral imager (THI), an airborne hyperspectral imager (AVIRIS-NG), and a space-borne multispectral imager (Sentinel-2). We used a point-based spectroradiometer and pixel-based THI to collect the in-situ reference target reflectance spectra and generated a radiance spectral library by simulating TOA radiance spectra using the Second Simulation of the Satellite Signal in the Solar Spectrum (6S) radiative transfer model. We have considered two cases of target radiance simulations, i.e., (i) corresponding to a grid of different AOT values for a predefined atmospheric and aerosol profile, and (ii) corresponding to varying combinations of atmospheric and aerosol profiles at a given AOT. The detection has been carried out using multiple target detection algorithms. Results indicate that the spectral knowledge-based targets can be detected in remote sensing data under different atmospheric model scenarios using the FM approach. A detection rate of about 75% and 50% have been consistently obtained for remote sensing data from airborne and space-borne platforms with a false alarm (FA) rate of 10^{-2} to 10^{-3} respectively. Change in the AOT across atmospheric models has resulted in decision-changing implications in the target detection modeling. The selection of the wrong atmospheric profile can potentially aggravate the number of FAs produced by a particular detection algorithm.

1. Introduction

Current optical remote sensors facilitate data capture at a high spatial and spectral resolution, thereby aiding material identification at a finer scale. This advancement has led to the use of optical remote sensing data for solving several recurrent problems in remote sensing applications such as target detection (Geng et al., 2016; Xu et al., 2017), classification (Cheng et al., 2017; Lu et al., 2017), change detection (Hussain et al., 2013; Tewkesbury et al., 2015), anomaly detection (Qu et al., 2017; Taghipour and Ghassemian, 2017), etc. Target detection using optical remote sensing data has gained substantial attention in the last decade in various applications in defense (Briottet et al., 2006), security, surveillance (Yuen and Richardson, 2010), agriculture (Chen et al., 2019), etc. Target detection refers to detecting sparsely distributed

* Corresponding author at: Department of Earth and Space Sciences, Indian Institute of Space Science and Technology, Valiamala, Thiruvananthapuram, Kerala, India.
E-mail addresses: sudhanshushekhar88@gmail.com (S.S. Jha), rao@iist.ac.in (R.R. Nidamanuri), emmett@cis.rit.edu (E.J. Ientilucci).

https://doi.org/10.1016/j.isprsjprs.2021.11.011
Received 8 May 2021; Received in revised form 20 October 2021; Accepted 12 November 2021

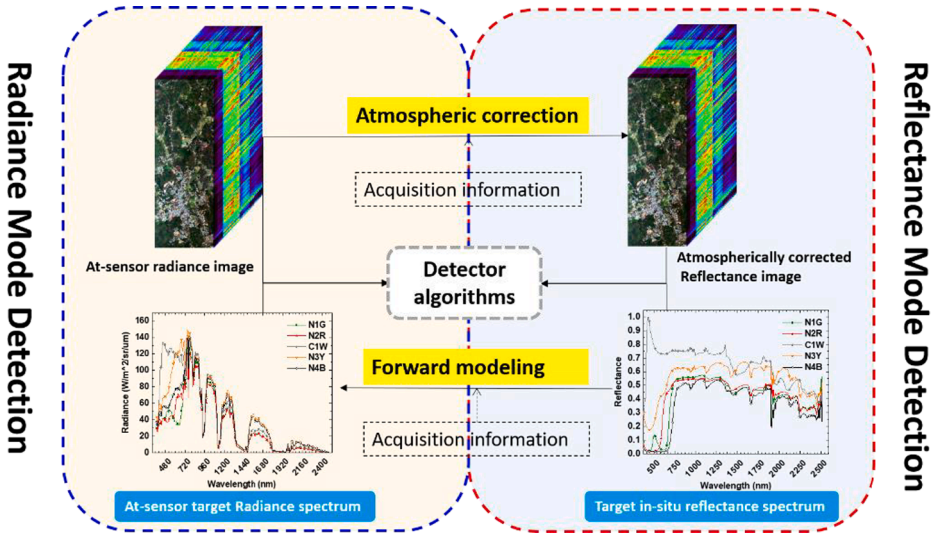

Fig. 1. Target detection domains.

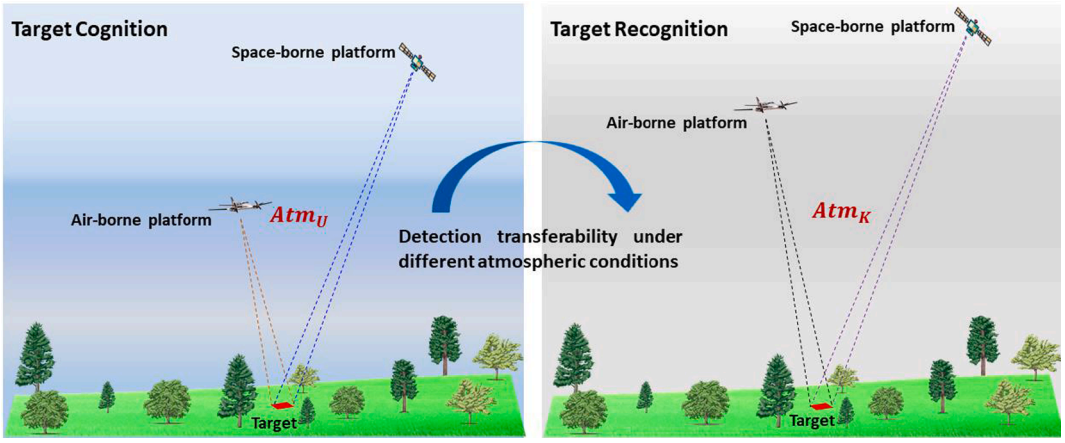

Fig. 2. Two different space–time target detection scenarios, with differing atmospheric conditions (Atm_U, Atm_K), leading to a potential mismatch of atmospheric parameters.

engineered objects/materials (e.g., 5 to10 pixels out of a million) in the imagery. The sparse nature of targets combined with the propagations of uncertainties in the imaging process, such as sensor noise, atmospheric scattering, absorption, target surface characteristics, etc., deters or hinders a reliable detection rate. Target detection from remote sensing platforms such as unmanned aerial vehicles (UAVs), airborne flights, etc., requires a multi-dimensional approach to improve detection accuracy, including mitigation of uncertainties caused by inefficient atmospheric parameter modeling. There have been a few studies on the effect of various factors such as the size of the target, target-background interaction, sensor characteristics, algorithms, etc., (Wang and Xue, 2017; Yadav et al., 2018) on target detection performance. Still, the impact of the radiative transfer model (RTM)-based estimates of the atmospheric variables such as standard atmospheric profiles, aerosol models, etc., and associated uncertainties related to target detection performance has been overlooked and, in general, reported less in the literature (Yarbrough et al., 2010; Sundberg, 2018; Kim et al., 2019).

Usually, the target detection chain involves RTM (Fig. 1) in the image pre-processing stages to compensate for the atmospheric effects (i.e., scattering and absorption of the signal) from the measured at-sensor radiance. Such a process is termed atmospheric correction or compensation (AC) or inverse modeling (IM) and is generally carried out using physics-based models such as MODerate resolution atmospheric TRANsmission (MODTRAN), Second Simulation of the Satellite Signal in the Solar Spectrum (6S) (Ientilucci and Bajorski, 2006; Ientilucci and Adler-Golden, 2019). It is common to use the AC mode of data pre-processing for numerous remote sensing applications (Agapiou et al., 2011; Martins et al., 2017). The AC approach for quantifying remote sensing products involves intensive computing resources (big remote sensing data) and is often time-consuming (pixel by pixel inversion), a bottleneck for decision-makers. An alternative approach, forward-modeling (FM), uses in-situ reflectance data of the objects at the ground to approximate their at-sensor spectral radiance (Matteoli et al., 2009; Ayhan and Kwan, 2017; Ientilucci, 2017). The FM approach requires less computational resources as the modeling process is limited to generating a few spectral vectors corresponding to a gamut of atmospheric parameters, unlike the AC approach, which would require the generation of several data cubes for the same (Matteoli et al., 2010).

Physics-based models typically require multiple parameters to approximate the atmosphere, such as columnar temperature, pressure, water vapor, ozone, gaseous transmittance, scattering model, aerosol optical thickness, etc. The reliability of remote sensing-based studies depends upon the quality of estimation of these atmospheric parameters (Nia et al., 2015; Marcello et al., 2016; Sabater et al., 2017; Seong et al., 2020). In terms of data models and hardware capability, substantial developments in computing infrastructure have encouraged researchers

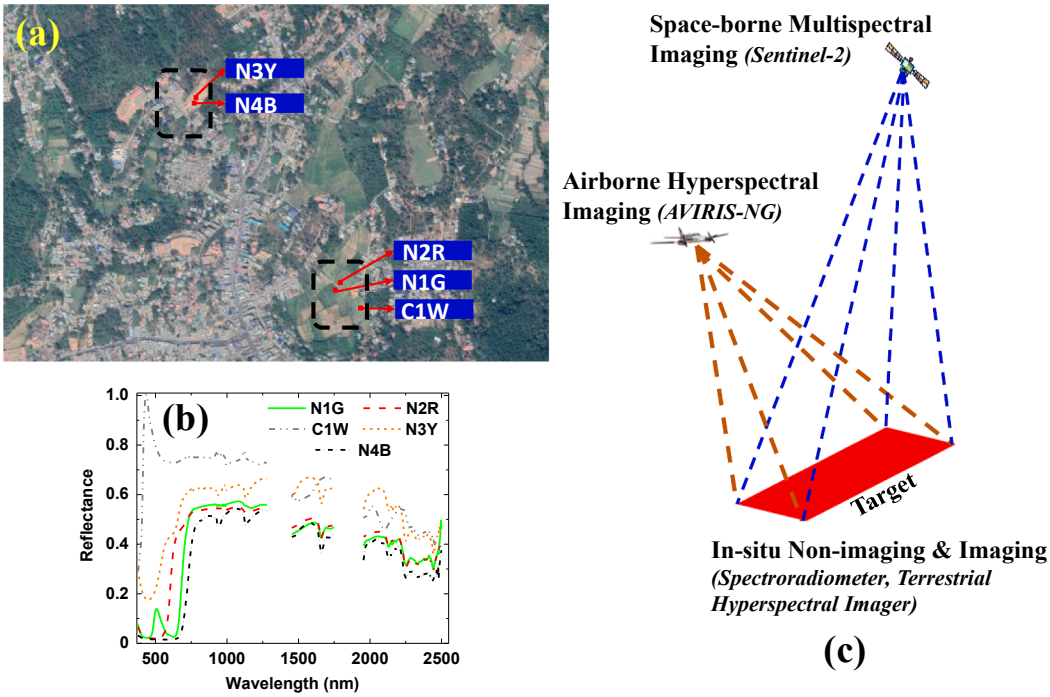

Fig. 3. Experimental setup of the Gudalur spectral target-detection (GST-D) dataset with (a) target positions as seen from Google Earth imagery for the targets – N1G, N2R, C1W, N3Y, and N4B (b) respective in-situ target reflectance spectra, and (c) the experimental multi-platform target acquisition setup used in this paper (Adapted from Jha et al., 2020).

to explore efficient methods to expedite onboard methods for various recurrent problems in remote sensing (Bue et al., 2015). Although some studies have been reported on onboard AC, their scope remains limited due to the exhaustive resource required for such implementations. On the other hand, accelerated hardware components such as FPGA have shown that real-time applications, such as object detection and classification, can be carried out given computational overheads are optimized (Gyaneshwar and Nidamanuri, 2020; Nascimento et al., 2020). One of the limiting factors for carrying out such operations is uncertainties in modeling the atmospheric parameters. Although few studies have analyzed the impact of modeling the atmospheric parameters on remote sensing-derived products, exhaustive studies have been less reported in the literature. A study by Matteoli, Ientilucci, and Kerekes (2010) has laid out a detailed analysis of the computational and operational aspects of the FM approach for target detection. They simulated different radiance spectra (81 in total) for various geometric and illumination parameters. But atmospheric variability parameters such as atmospheric models and aerosol models were not tested or evaluated. Axelsson et al. (2016) implemented the FM method for target detection but used in-scene information rather than the physics-based RT models to derive target information. Also, the dataset used in that study had a limited spectral channel range (400–1000 nm) acquired from an altitude of only1000 m, which inhibits observable effects of atmospheric variables on target detection performance.

The objective of this research is a critical analysis of the performance of target detection in multi-platform hyperspectral and multispectral imagery under different atmospheric models and parameter scenarios. A hypothetical situation, illustrated in Fig. 2, in which the target cognition-recognition cycle becomes an integral part of such a framework's overall applicability arises in an onboard target detection framework. Target cognition refers to the first instance of target information (spectral characteristics) acquisition; target recognition refers to the usage of spectral information acquired in the cognition stage to identify the target thereafter. This work aims to 1) analyze the impact the atmospheric model has on target detection, and 2) assess the applicability of the FM approach for target detection in a multi-platform target detection dataset. We have modeled the atmospheric variables using the 6S RT model and transformed the in-situ target reflectance spectra to at-sensor radiance spectra using standard atmospheric models containing pre-computed estimates of the atmospheric parameters. Finally, we carried out target detection using various state-of-the-art target detectors and compared the results for all the combinations of atmospheric state variables and algorithms.

2. Materials and methods

2.1. Target data acquisition experiment

We designed a multi-platform image acquisition setup in which the targets were acquired concurrently using a ground-based terrestrial hyperspectral imager (THI), an airborne hyperspectral imager (AVIRIS-NG) (Bhattacharya et al., 2019), and a space-borne multispectral imager (Sentinel-2), as shown in Fig. 3. In this experiment, AVIRIS-NG captured imagery with 4 m spatial resolution at 5 nm spectral resolution in the 400–2500 nm wavelength range with 425 channels. THI is a push-broom hyperspectral imager (Headwall Photonics Inc., USA) that captures imagery in the VNIR (400–1000 nm) range of electromagnetic spectrum with 837 channels sampled at 1 nm interval. The experiment was carried out on a natural landscape area on 18th March 2018 at Gudalur city, located in Tamilnadu, India. Five artificial nylon and cotton sheet targets, designated as N1G (green nylon sheet), N2R (red nylon sheet), C1W (white cotton sheet), N3Y (yellow nylon sheet), and N4B (black nylon sheet) (Jha et al., 2020), each of size 10 × 10 m, were used for the experiment. Targets N1G and N3Y were placed on grass and soil backgrounds, respectively, to introduce a natural camouflage scenario in the visible (400–700 nm) portion of the electromagnetic spectrum. Further, targets such as N1G, N2R, N3Y, and N4B have similar spectral characteristics (same nylon material), which provide an opportunity to test the reproducibility of detection performance of similar material by different algorithms. The spatial location of the targets was recorded using a GPS device. As the target panel size is relatively larger than the pixel size for airborne imagery, for each target, we marked a 16-pixel region of

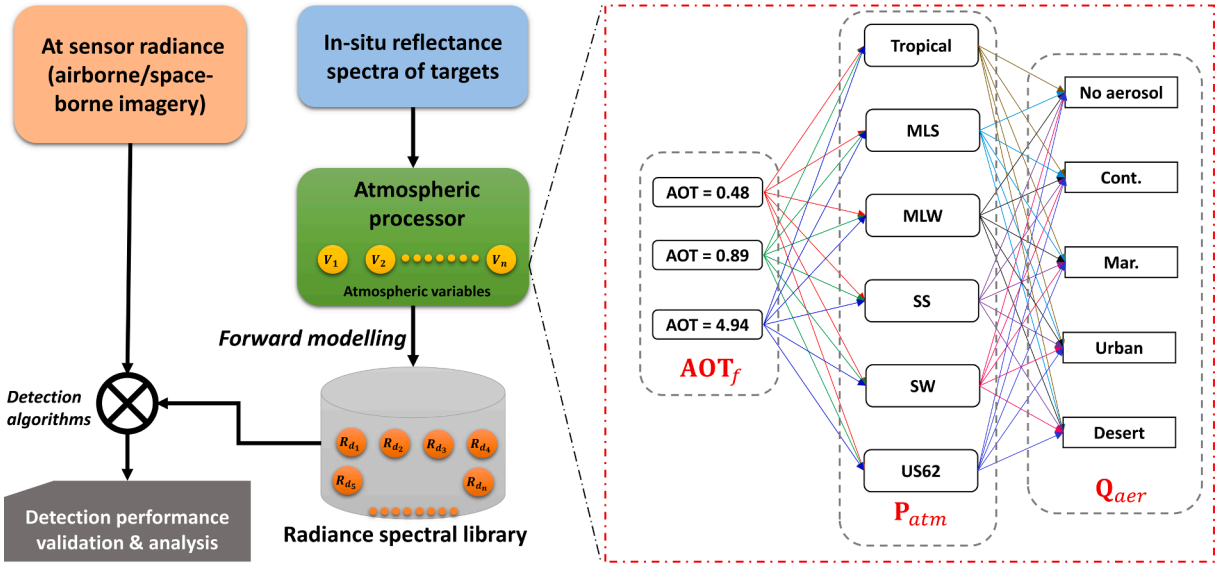

MLS : midlatitude summer; **MLW :** midlatitude winter; **SS :** subartic summer; **SW :** subartic winter; **Cont. :** continental; **Mar. :** Maritime

Fig. 4. 6S RT model-based target modeling system design for evaluating spectral target detection performance in multi-platform remote sensing imagery setup.

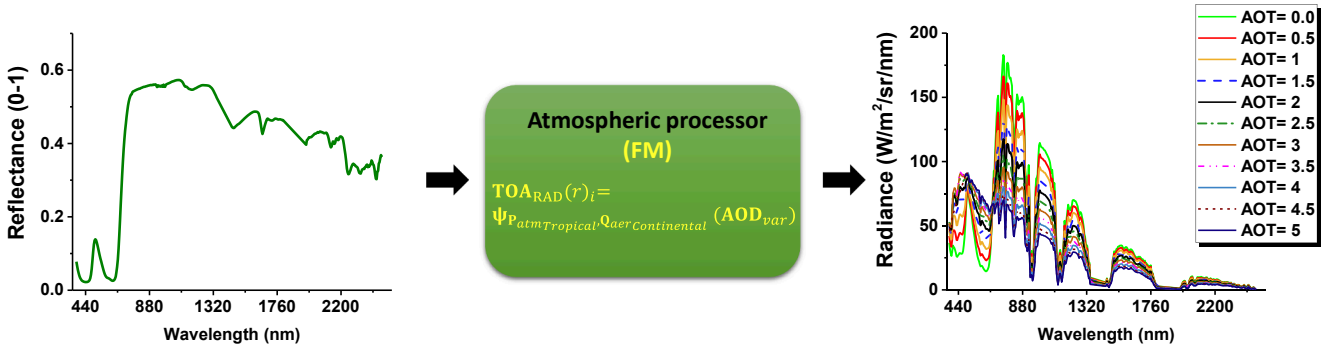

Fig. 5. FM approach for simulation of the N1G target radiance spectra using Eq. (5) for various AOT values using the in-situ reflectance spectra.

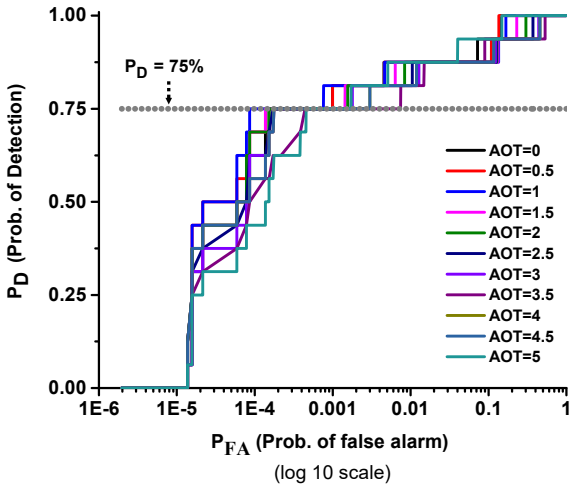

Fig. 6. An example target detection result for the N1G target under varying AOT conditions by the MF target detection algorithm.

interest (ROI) as the target footprint as recommendations by Manolakis et al. (2003). In the case of space-borne imagery, 4-pixel ROI was marked for N1G, N2R, N3Y, and N4B. For the target C1W, 6-pixel ROI was marked in space-borne imagery for C1W as a greater number of pixels were diffused and appeared as target due to distinct imaging geometry. Moreover, due to different spatial resolutions of airborne and space-borne imagery, the ROI in space-borne imagery may also contain sub-pixel target material. The targets were acquired from platforms with different operational altitudes (airborne: ~ 4–6 km and space-borne: ~705 km) to gauge the two different sets of concomitant atmospheric conditions allowing us to assess atmosphere-induced uncertainty in the target detection process.

2.2. *Data pre-processing: Reference target spectra and imagery pre-processing*

We deployed two different hyperspectral sensing instruments: a point-based spectroradiometer and a pixel-based THI to collect the in-situ reference target reflectance spectra. Although the THI captures imagery at about 1 cm spatial resolution, we spatially resampled imagery to 20 cm spatial resolution. The THI raw data were calibrated using a white reference panel to obtain the radiance data cube and subsequently converted to reflectance cube using the in-scene empirical line (EL) method (Smith and Milton, 1999). Different patches over the target were selected, and spectral responses were averaged to yield a THI in-situ target spectrum. In addition, we collected point-based in-situ target spectra in the 400–2500 nm wavelength range using a field spectroradiometer (Spectra Vista Corporation, HR-1024i, USA) (Field

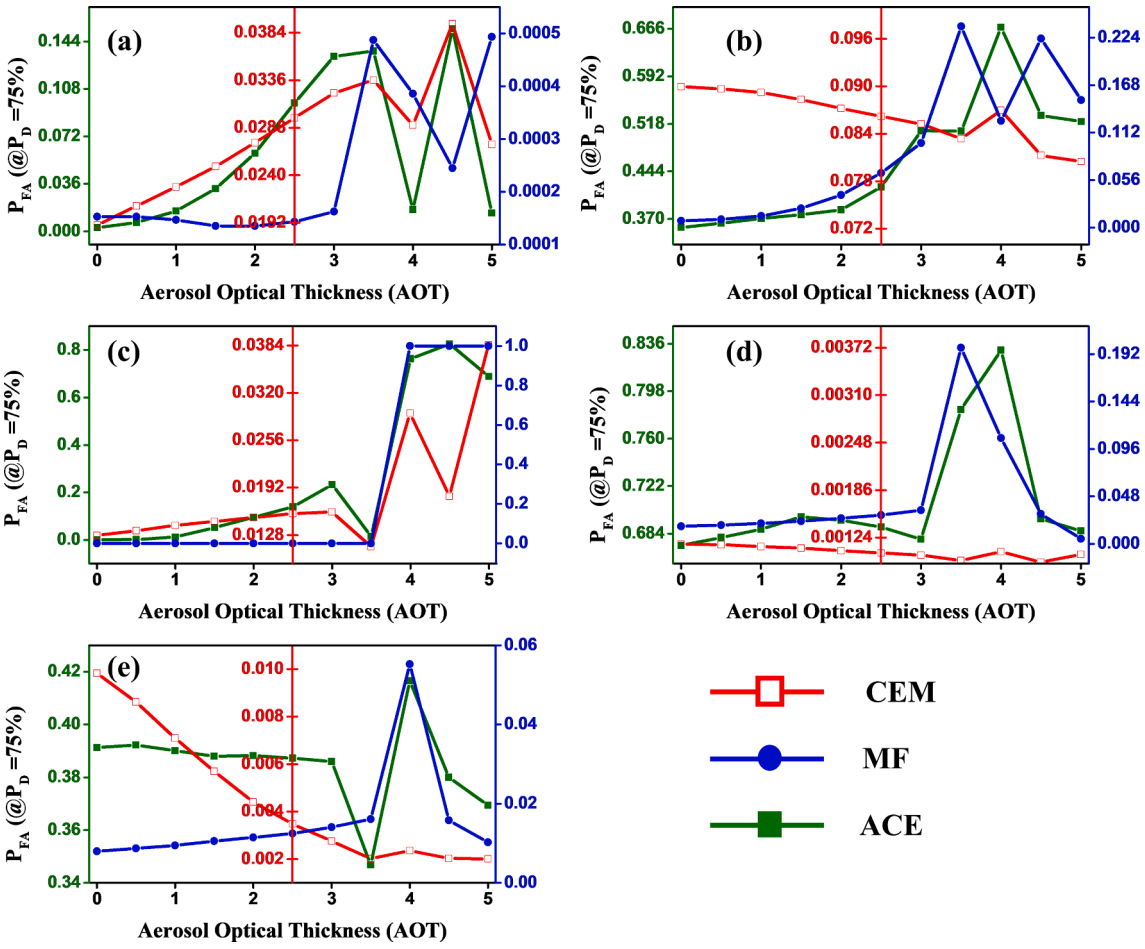

Fig.7. Target detection in airborne imagery: variation of P_{FA} due to changes in AOT for target detection in airborne imagery. Illustrated are P_{FA} values when the P_D = 75% for targets (a) N1G, (b) N2R, (c) C1W, (d) N3Y, and (e) N4B with simulated TOA target radiance spectra at different AOT values between 0 and 5 using the point-based target reflectance.

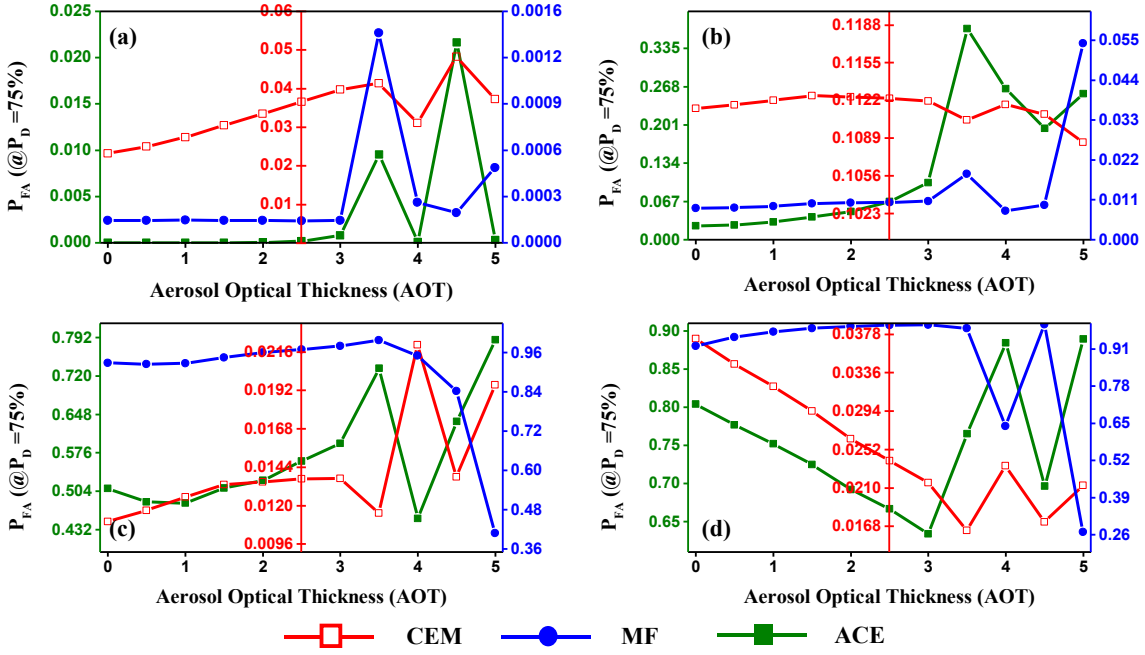

Fig. 8. Airborne imagery detection results. Illustrated are P_{FA} values when the P_D = 75% for targets (a) N1G, (b) N2R, (c) C1W, (d) N3Y, and (e) N4B with simulated TOA target radiance spectra at different AOT values between 0 and 5 using the pixel-based THI target reflectance.

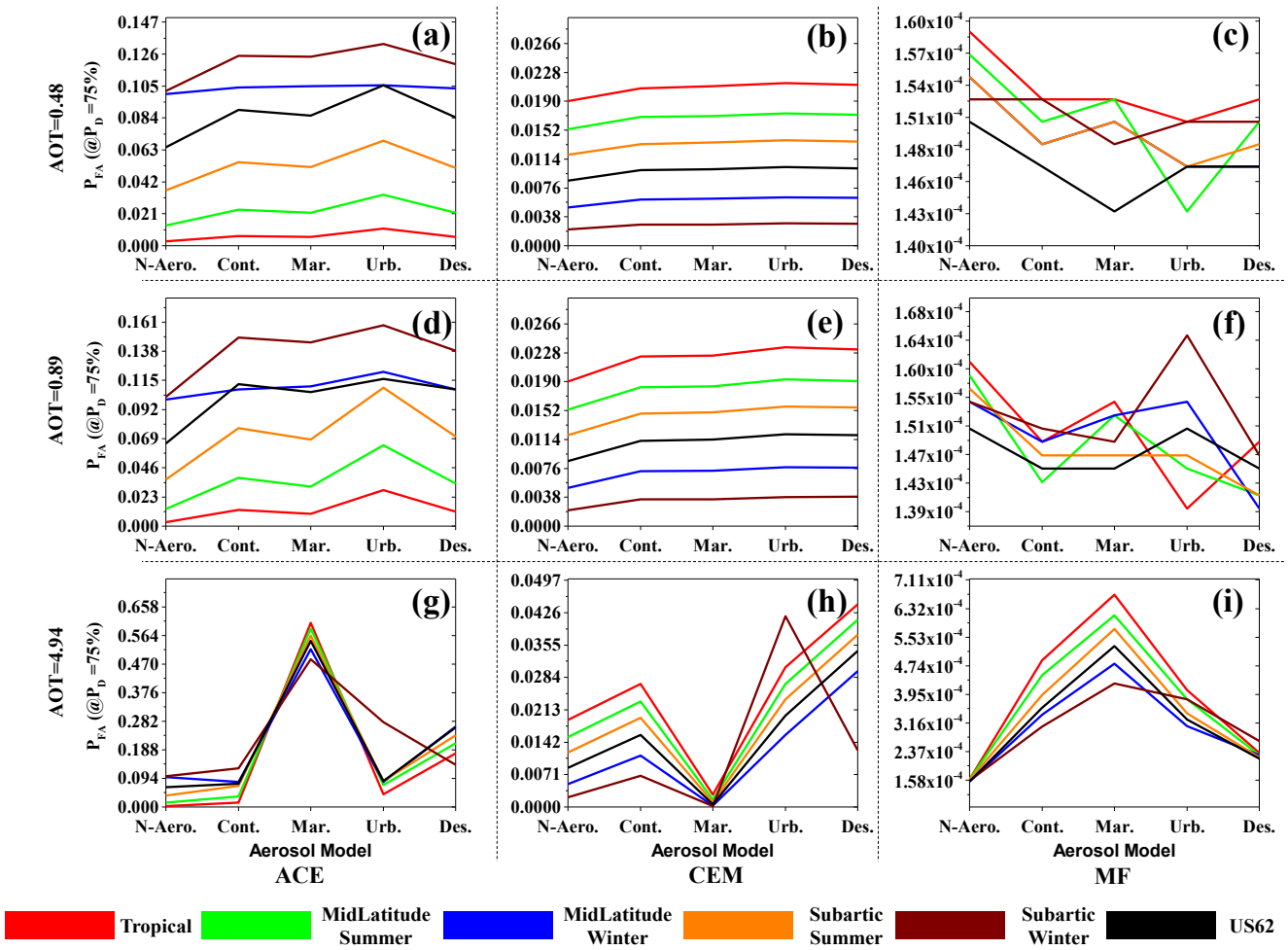

Fig. 9. Airborne imagery detection results. Illustrated are P_{FA} values when the P_D = 75% for the N1G target with simulated TOA target radiance spectra at (a-c) AOT = 0.48, (d-f) AOT = 0.89, and (g-i) AOT = 4.94 for different standard aerosol models (N-Aero. = No Aerosol, Cont. = Continental, Mar. = Maritime, Urb. = Urban, Des. = Desert) and atmospheric models (i.e., colored line) using the point-based target reflectance.

Spectroscopy Guide with SVC i-series Spectroradiometers, 2010) and further processed the spectra to match to the spectral range of AVIRIS-NG and Sentinel-2 sensors via spectral resampling and convolution operation using the respective sensor response function (SRF). In the target spectral data acquired using the THI sensor, we omitted data beyond 900 nm due to inherent sensor noise and low signal-to-noise ratio (SNR). In the case of THI-based input target reference spectra, we resampled the AVIRIS-NG imagery to THI wavelength range which resulted in imagery with 104 spectral bands for target detection.

Since we used forward modeled target spectra for detection in this experiment, the target imagery needed to be of the top-of-atmosphere (TOA) radiance. For this, we used the level-1 TOA radiance product of Sentinel-2 by converting the original level L1C (TOA reflectance) to TOA radiance using the Sentinel application platform (SNAP) tool processor called Sen2Cor (Louis et al., 2016). The AVIRIS-NG data is available as TOA radiance data and thus needs no pre-processing such as radiometric calibration or atmospheric correction steps. However, we removed the bands in the water vapor absorption region of the AVIRIS-NG imagery between 1348 and 1443 nm, 1804–1954 nm, and 2485–2500 nm. The resultant imagery contained 370 spectral bands. We resampled the Sentinel-2 satellite imagery to 10 m spatial resolution to match the target size.

2.3. Target signal simulation: Atmospheric processor

Since electromagnetic (EM) radiation in the optical region undergoes perturbation caused by atmospheric components such as aerosols, water vapor, clouds, dust, etc., various physics-based RTMs need to be used to approximate different parameters to compensate for the net atmospheric effects. The 6S radiative transfer code models the electromagnetic radiation in the 400 to 2500 nm range of the EM spectrum. The governing equation for estimating surface reflectance reaching a remote sensor is:

$$\rho^{*}_{toa} = \frac{\pi^{*} L_{TOA}}{\mu_s E_s}, \tag{1}$$

where ρ^{*}_{toa} is the top-of-atmosphere reflectance, L_{TOA} is the TOA radiance, μ_s is the cosine of the solar zenith angle, and E_s is the TOA solar flux. Considering the scattering (Rayleigh and Mie) and absorption of radiation reaching the sensor, for a simplified case of uniform a Lambertian surface, Eq. (1) can be written as:

$$\rho^{*}_{toa}(\theta_s, \theta_v, \varphi_s, \varphi_v) = T_g(\theta_s, \theta_v)\left[\rho_a + T(\theta_s)T(\theta_v)\frac{\rho_{ac}}{1 - S_a \times \rho_{ac}}\right], \tag{2}$$

where θ_s, θ_v and φ_s, φ_v are the geometrical parameters (zenith and azimuth angles for solar and view positions of sun and sensor, respectively), ρ_a is the atmospheric path radiance, T_g is the gaseous transmittance, $T(\theta_s)$ is the transmittance from the sun to the ground, $T(\theta_v)$ is the transmittance from the ground to the sensor, S_a is the spherical albedo and ρ_{ac} is the atmospherically corrected surface reflectance, also known as bottom-of-atmosphere (BOA) reflectance.

The 6S RTM incorporates various standard atmospheric models

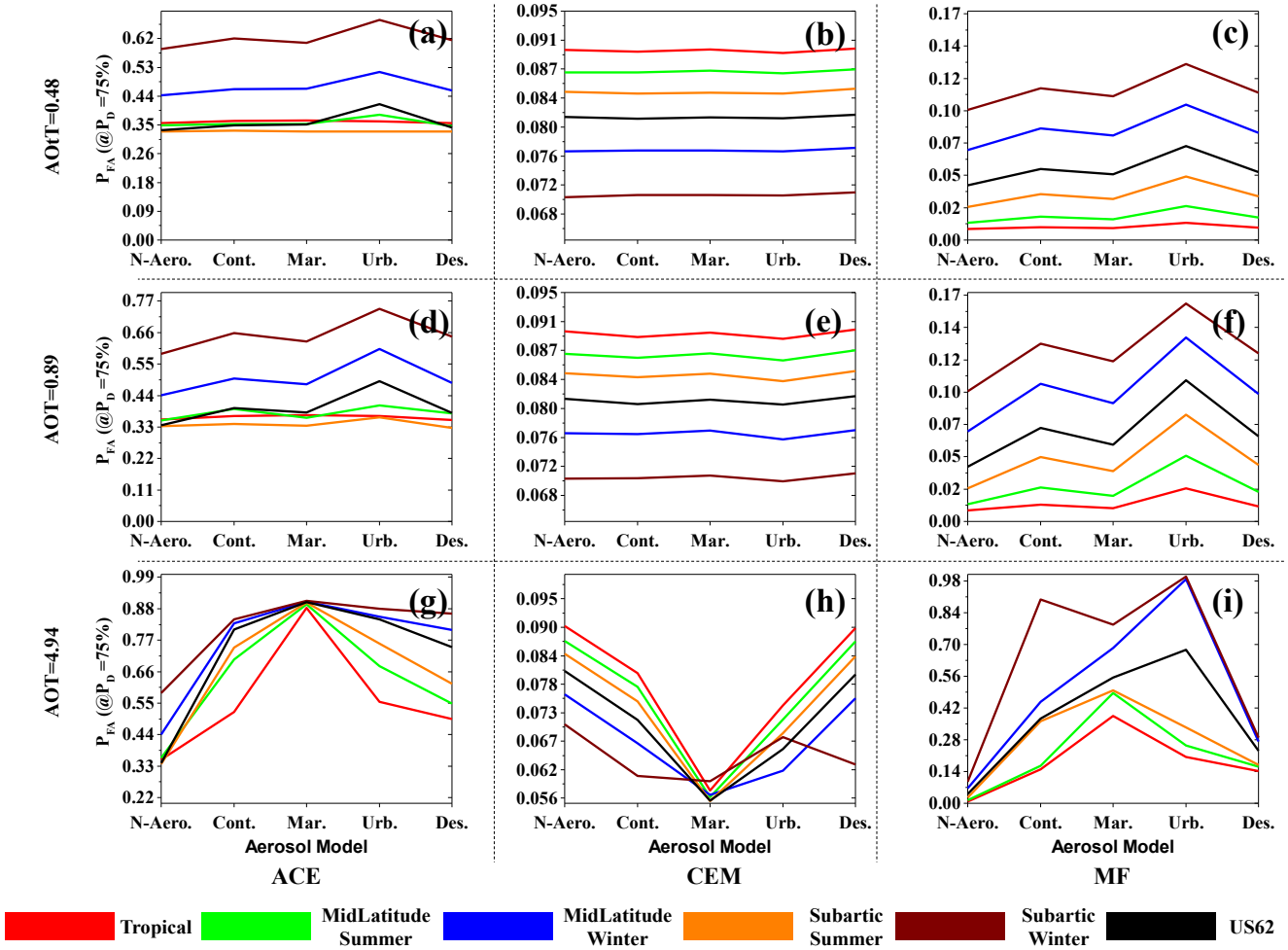

Fig. 10. Airborne imagery detection results. Illustrated are P_{FA} values when the $P_D = 75\%$ for the N2R target with simulated TOA target radiance spectra at (a-c) AOT = 0.48, (d-f) AOT = 0.89, and (g-i) AOT = 4.94 for different standard aerosol models (N-Aero. = No Aerosol, Cont. = Continental, Mar. = Maritime, Urb. = Urban, Des. = Desert) and atmospheric models (i.e., colored line) using the point-based target reflectance.

defined by approximation of climatic conditions, such as Tropical, Midlatitude Summer, etc. The atmospheric profiles have predefined columnar profiles (0–100 km) of different variables such as atmospheric pressure (mb), temperature (^{o}K), water vapor (g/m^3), and ozone concentrations (g/m^3) as a function of height (km). Further, based on aerosol properties such as aerosol optical thickness (AOT), the mean radius of the aerosol particle, real/imaginary refractive indices, particle distribution function, and angstrom coefficient, several standard aerosol models (continental, urban, maritime, desert, etc.) are also defined in the 6S model. Taking into account for these variables explicitly as a function of wavelength λ, Eq. (2) can be modified as:

$$\rho^{\lambda}_{toa}\left(\theta_s,\theta_v,\varphi_s,\varphi_v,P,\psi^{\lambda},U_{H_2O},U_{O_3}\right)=T^{\lambda}_{g_{OG}}(m,P)T^{\lambda}_{g_{O_3}}\left(m,U_{O_3}\right)\left[\rho^{\lambda}_{a}\left(\theta_s,\theta_v,\varphi_s,\varphi_v,P,\psi^{\lambda},U_{H_2O}\right)+T^{\lambda}_{r_a}\left(\theta_s,\theta_v,\varphi_s,\varphi_v,P,\psi^{\lambda}\right)\frac{\rho_{ac}}{1-S^{\lambda}_{a}(P,\psi^{\lambda})\rho_{ac}}T^{\lambda}_{g_{H_2O}}(m,U_{H_2O})\right], \quad (3)$$

where P is the atmospheric pressure (mb), U_{H_2O} is the integrated atmospheric water vapor (cm), U_{O_3} is the integrated columnar ozone concentration (cm-atm), m is the air-mass given as $\frac{1}{\cos\theta_s}+\frac{1}{\cos\theta_v}$, $T_{g_{OG}}$, $T_{g_{H_2O}}$ and $T_{g_{O_3}}$ represent the gaseous transmittance by gases like $OG=\{CO_2, O_2, CH_4\}$, water vapor (H_2O) and ozone (O_3) respectively; ψ^{λ} represents the aerosol components described as:

$$\psi^{\lambda}=(\tau_a,\omega_0,\mathrm{P}_a), \quad (4)$$

where τ_a is the AOT, ω_0 is single scattering albedo and P_a is the phase function at a given wavelength λ.

Inverting Eq. (1), we have:

$$L_{TOA}=\frac{\rho^{*}_{toa}\times\mu_s E_s}{\pi}, \quad (5)$$

where $\rho^{*}_{toa}=\rho^{\lambda}_{toa}$ and is given by Eq. (3). Since the values of ρ_{ac} for the targets are known a priori from the in-situ measurements, we can simulate L_{TOA} reaching the sensor owing to different atmospheric variables using Eq. (3). The radiance spectral library was constructed by multiple runs of the 6S code using the in-situ target surface reflectance. A schematic diagram of the overall process is shown in Fig. 4.

We considered two cases of target radiance spectra simulations: (i) simulation corresponding to a grid of different AOT values (0–5) for a

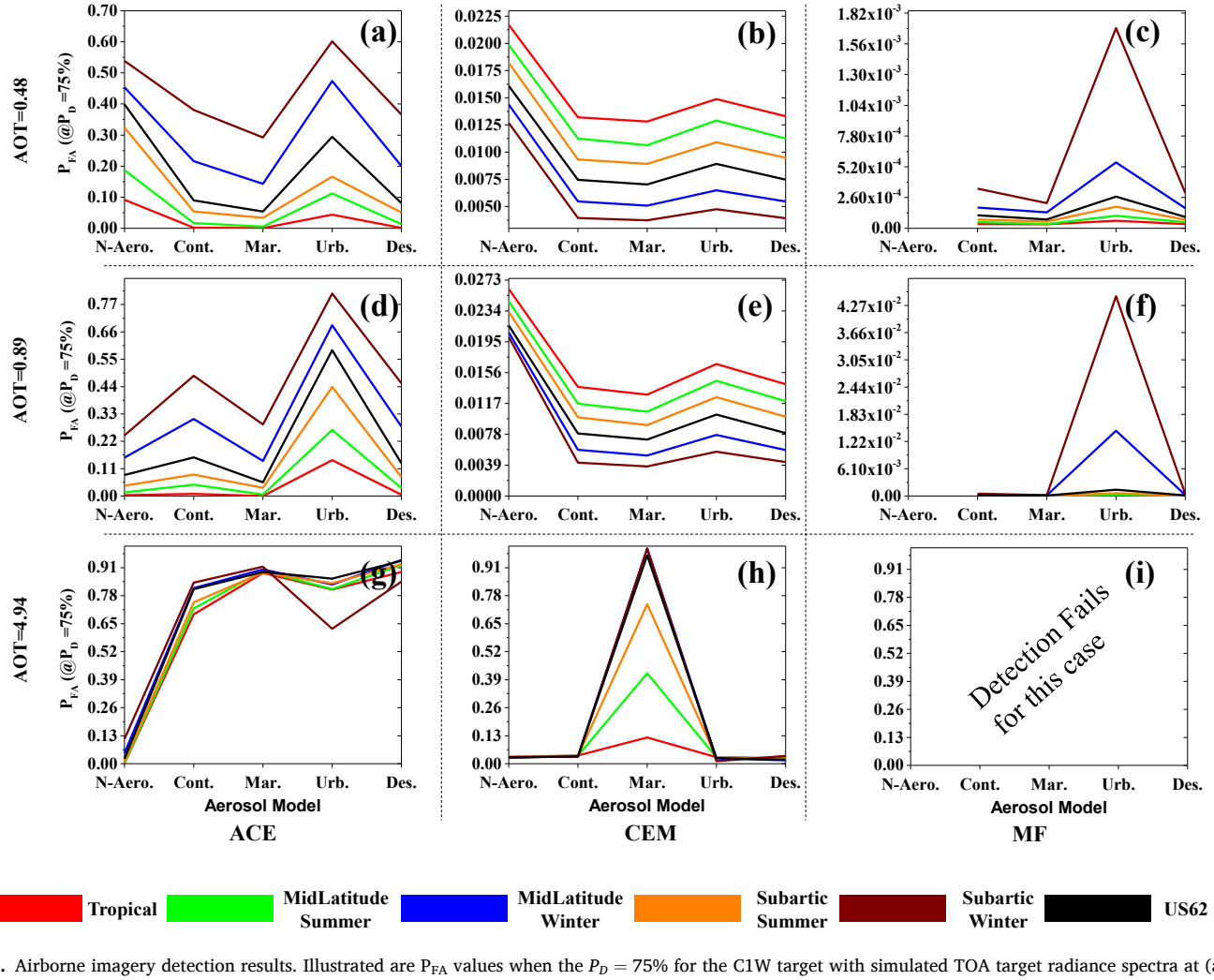

Fig. 11. Airborne imagery detection results. Illustrated are P_{FA} values when the $P_D = 75\%$ for the C1W target with simulated TOA target radiance spectra at (a-c) AOT = 0.48, (d-f) AOT = 0.89, and (g-i) AOT = 4.94 for different standard aerosol models (N-Aero. = No Aerosol, Cont. = Continental, Mar. = Maritime, Urb. = Urban, Des. = Desert) and atmospheric models (i.e., colored line) using the point-based target reflectance.

predefined atmospheric (Tropical) and aerosol (Continental) profile and (ii) simulation corresponding to different combinations of atmospheric and aerosol profile at a given AOT's = {0.48,0.89,4.94} corresponding to equivalent visibility of approximately 15 km, 7 km, and 1 km respectively (Bhatia et al., 2018). Considering the geographical location of the target scene (Tamil Nadu, India), a tropical atmospheric profile with a continental aerosol model were selected (Mishra et al., 2020) for the predefined parameters of the case (i). Denoting different atmospheric profiles as $\mathbf{P}_{atm}$ = {Tropical, Midlatitude Summer, Midlatitude Winter, Subartic Summer, Subartic Winter, US62}, aerosol profiles as $\mathbf{Q}_{aer}$ = {No aerosol, Continental, Maritime, Urban, Desert), TOA radiance $\mathbf{TOA}_{\mathrm{RAD}}(r)_i$, for case (i) is represented as:

$$\mathbf{TOA}_{\mathrm{RAD}}(r)_i = \psi_{\mathbf{P}_{atm\,Tropical},\mathbf{Q}_{aer\,Continental}}(\mathbf{AOT}_{var}), \tag{6}$$

where,

$\mathbf{AOT}_{var} = \{0, 0.5, 1, 1.5, 2, 2.5, 3, 3.5, 4, 4.5, 5\}$, and subscript i = values of TOA radiance at different AOT values.

An example illustrating the simulated radiance spectra from the atmospheric processor following Eq. (6) is shown in Fig. 5.

Further, $\mathbf{TOA}_{\mathrm{RAD}}(r)_i$ for case (ii) at different discrete values of AOT is given as:

$$\mathbf{TOA}_{\mathrm{RAD}}(r)_i = \psi_{\mathbf{AOT}_f}\left(\mathbf{P}_{atmp}, \mathbf{Q}_{aerq}\right), \tag{7}$$

where, $\mathbf{AOT}_f = \{0.48, 0.89, 4.94\}$, subscripts p and q represent different atmospheric and aerosol profiles.

2.4. Target detection algorithms

Mathematically, spectral target detection is formulated as a binary hypothesis testing problem. Null hypothesis H_0 refers to the absence of the target, whereas the alternative hypothesis H_1 refers to target present. If we represent an image as $I_{(m\times n)}$ with m rows, n columns, and k bands or spectral channels such that each pixel $\mathbf{x}_{i=1}^{k} \in I_{k,mn}$, then for an assumption of a multivariate normal distribution of target and background (non-target pixels), the target detection problem can be expressed as:

$$\begin{aligned} H_0 &: \mathbf{x} = \mathbf{n} \\ H_1 &: \mathbf{x} = \mathbf{s} + \mathbf{n}, \end{aligned} \tag{8}$$

where $\mathbf{n} \sim N(\boldsymbol{\mu}, \boldsymbol{\Sigma})$ is the noise or background with a mean ($\boldsymbol{\mu}$) and covariance matrix ($\boldsymbol{\Sigma}$) as distribution parameters; $\mathbf{s}$ is the known target sample spectrum. Targets can occupy either a full or partial pixel. If the target occupies one complete pixel, it is considered a full pixel, and the statistical detectors for this scenario are generally governed by the hypothesis stated in Eq. (8). For sub-pixel target detection, the hypothesis is modified as:

$$\begin{aligned} H_0 &: \mathbf{x} = \mathbf{n} \\ H_1 &: \mathbf{x} = \alpha\mathbf{s} + \beta\mathbf{n}, \end{aligned} \tag{9}$$

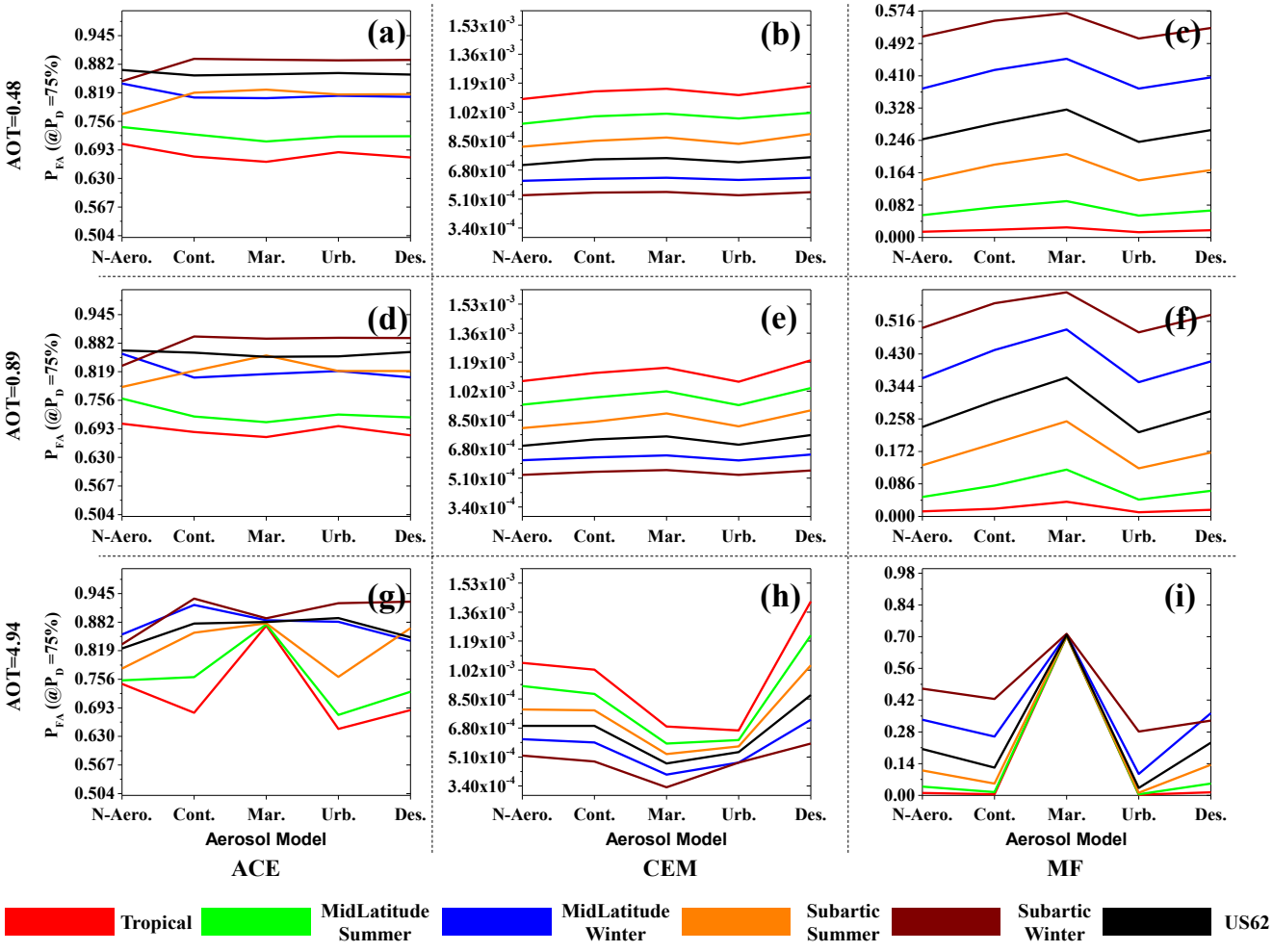

Fig. 12. Airborne imagery detection results. Illustrated are P_{FA} values when the $P_D = 75\%$ for the N3Y target with simulated TOA target radiance spectra at (a-c) AOT = 0.48, (d-f) AOT = 0.89, and (g-i) AOT = 4.94 for different standard aerosol models (N-Aero. = No Aerosol, Cont. = Continental, Mar. = Maritime, Urb. = Urban, Des. = Desert) and atmospheric models (i.e., colored line) using the point-based target reflectance.

where $\mathbf{x} \sim N(\mathbf{0}, \mathbf{\Sigma})$ under H_0 and $\mathbf{x} \sim N(\alpha\mathbf{s}, \beta^2\mathbf{\Sigma})$ under H_1, α refers to the fill fraction of the target or abundances if $\mathbf{s}$ represents a matrix containing endmembers. Since targets in this experiment fall under both the full-pixel and sub-pixel categories, we used the matched filter (MF), adaptive cosine estimator (ACE), and constrained energy minimization (CEM) detectors. Several sophisticated and advanced target detection algorithms have been proposed in the literature, such as kernel-based methods (Wang et al., 2013; Kwan et al., 2020)), machine learning methods (Zhang et al., 2014; Du and Li, 2018). However, since the objective of the paper is not the evaluation of target detection performance as a function of the choice of algorithms, we chose classical and robust detectors, which have been widely used in the research community. A detailed discussion on the detectors used in this work can be found in Manolakis et al. (2016); nonetheless, we provide a brief formulation of these detectors.

2.5. Matched filter (MF)

For a full-pixel target, the detection model described in Eq. (8) is modified as:

$$\begin{aligned} H_0 &: \mathbf{x} = \mathbf{n} \\ H_1 &: \mathbf{x} = \mathbf{s} + \alpha\mathbf{n}, \end{aligned} \tag{10}$$

where $\mathbf{n} \sim N(\boldsymbol{\mu}, \mathbf{\Sigma})$, and α is the unknown parameter. The detection model described by Eq. (11) is an additive model (Eismann, 2012) and assumes equal covariance ($\mathbf{\Sigma}$) under both the hypothesis H_0 and H_1. Estimating $\widehat{\boldsymbol{\mu}}$, $\widehat{\mathbf{\Sigma}}$, and $\widehat{\alpha}$ using the maximum likelihood estimation (MLE), we express the MF score r as:

$$r_{MF}(\mathbf{x}) = \frac{(\mathbf{s} - \widehat{\boldsymbol{\mu}})^T \widehat{\mathbf{\Sigma}}^{-1} (\mathbf{x} - \widehat{\boldsymbol{\mu}})}{\sqrt{(\mathbf{s} - \widehat{\boldsymbol{\mu}})^T \widehat{\mathbf{\Sigma}}^{-1} (\mathbf{s} - \widehat{\boldsymbol{\mu}})}}. \tag{11}$$

2.6. Adaptive cosine estimator (ACE)

For a sub-pixel target, the signal model for the ACE detector is based on replacement model (Manolakis, 2005) and is derived by modifying Eq. (9) as:

$$\begin{aligned} H_0 &: \mathbf{x} = \beta\mathbf{n} \\ H_1 &: \mathbf{x} = \alpha\mathbf{s} + \beta\mathbf{n}, \end{aligned} \tag{12}$$

where α, β are unknown parameters and $\mathbf{n} \sim N(\mathbf{0}, \mathbf{\Sigma})$. Unlike other signal models, where the covariance matrix $\mathbf{\Sigma}$ is assumed to be equal for both the null and alternate hypothesis, ACE assumes different $\mathbf{\Sigma}$ ($\mathbf{\Sigma_1}, \mathbf{\Sigma_2}$) and β for each of the hypotheses. Estimating the unknown parameters α, β_0, β_1, $\mathbf{\Sigma_1}$, and $\mathbf{\Sigma_2}$, ACE detector score is given by:

$$r_{ACE}(\mathbf{x}) = \frac{\left(\mathbf{x}^T \widehat{\mathbf{\Sigma}}^{-1} \mathbf{s}\right)\left(\mathbf{s}^T \widehat{\mathbf{\Sigma}}^{-1} \mathbf{s}\right)^{-1}\left(\mathbf{s}^T \widehat{\mathbf{\Sigma}}^{-1} \mathbf{x}\right)}{\left(\mathbf{x}^T \widehat{\mathbf{\Sigma}}^{-1} \mathbf{x}\right)}. \tag{13}$$

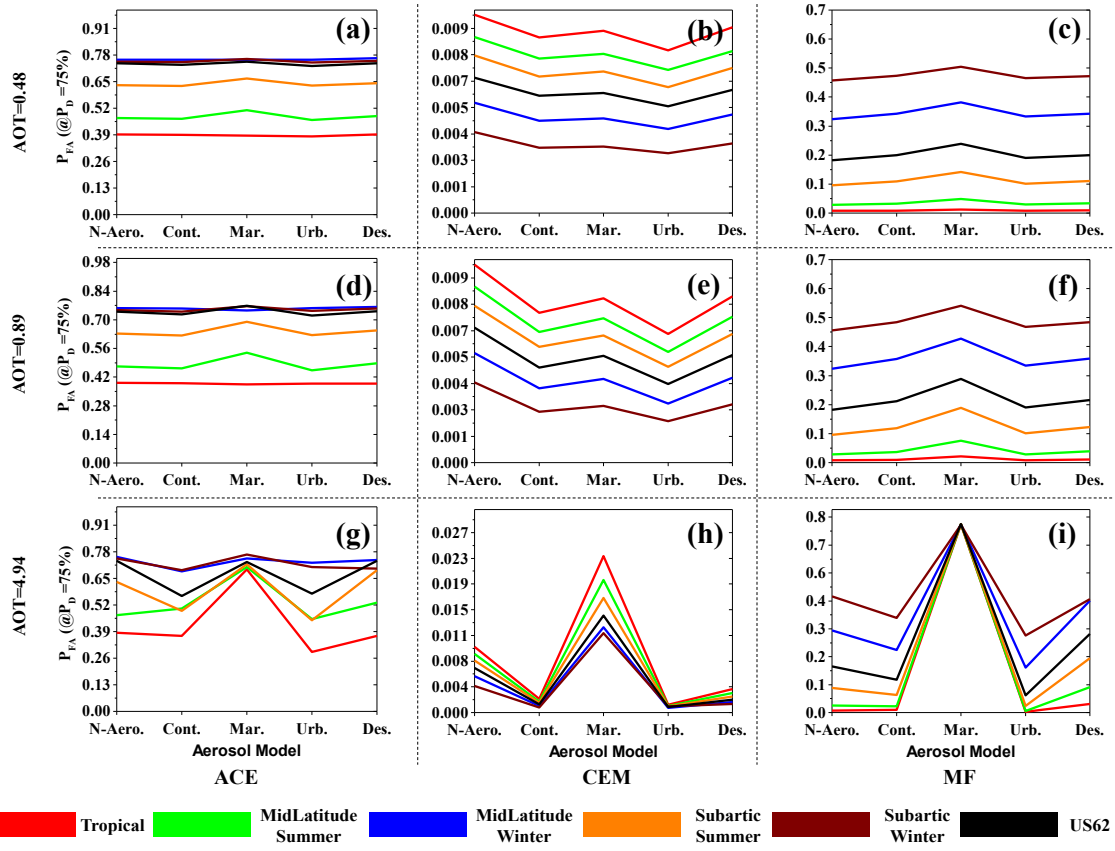

Fig. 13. Airborne imagery detection results. Illustrated are P_{FA} values when the $P_D = 75\%$ for the N4B target with simulated TOA target radiance spectra at (a-c) AOT = 0.48, (d-f) AOT = 0.89, and (g-i) AOT = 4.94 for different standard aerosol models (N-Aero. = No Aerosol, Cont. = Continental, Mar. = Maritime, Urb. = Urban, Des. = Desert) and atmospheric models (i.e., colored line) using the point-based target reflectance.

2.7. Constrained energy minimization (CEM):

Unlike the target detector models described, which assume a predefined statistical distribution of the target-background, the CEM detector operates independently of any deemed statistical distribution of the target-background subspace. CEM is based on energy minimization of the background pixel and is equivalent to a finite impulse response (FIR) filter and is given as:

$$r_{CEM}(\mathbf{x}) = \frac{(\mathbf{s}^{\mathrm{T}}\widehat{\mathbf{R}}^{-1}\mathbf{s})}{(\widehat{\mathbf{R}}^{-1}\mathbf{s})^{\mathrm{T}}\mathbf{x}}, \tag{14}$$

where $\widehat{\mathbf{R}}$ is the estimated background correlation matrix.

2.8. Quantitative evaluation of detection performance and spectral analysis

The target detection results using the algorithms considered from airborne and space-borne imagery were compared for all the simulated target reflectance spectra (shown as the radiance spectral library in Fig. 4). For reporting the detection performance, we used the receiver operating characteristic (ROC) curve, a graph between the probability of false alarm (P_{FA}) and the probability of detection (P_D) given as:

$$P_D = \frac{\text{Number of correctly identified target pixels}}{\text{Total number of actual target pixels}}$$
and
$$P_{FA} = \frac{\text{Number of pixels identified as false targets}}{\text{Total number of non} - \text{target pixels}}. \tag{15}$$

Furthermore, we performed a quantitative spectral analysis of the simulated target spectra comparing with the image-based target radiance spectra. The spectral analysis gives an insight into the underlying physical process that might result in a mismatch between image-derived target spectra and the input reference target spectra caused by a mismatch of the atmospheric model assumption. For each of the simulated target radiance spectra, we applied two widely used spectral matching metrics: spectral angle mapper (SAM) (Kruse et al., 1993) and spectral information divergence (SID) (Chang, 2000), and compared them with the image-derived (both from the airborne and space-borne platforms) target radiance. Given any two n-length vectors $\mathbf{A} = \{a_1, a_2, a_3, a_4 \cdots a_n\}^t$, and $\mathbf{B} = \{b_1, b_2, b_3, b_4 \cdots b_n\}^t$, SAM and SID are defined as:

$$\mathrm{SAM}(\mathbf{A},\mathbf{B}) = \cos^{-1}\left(\frac{\langle \mathbf{A},\mathbf{B}\rangle}{\|\mathbf{A}\|_2\|\mathbf{B}\|_2}\right), \tag{16}$$

where $\langle\rangle$ denotes the dot product of two vectors and $\|.\|_2$ denotes the Euclidean norm of a vector.

$$\mathrm{SID}(\mathbf{A},\mathbf{B}) = \mathrm{D}(\mathbf{A}||\mathbf{B}) + \mathrm{D}(\mathbf{B}||\mathbf{A}) = \sum_{i=1}^{n}\left(\frac{a_i}{\sum_{j=1}^{n}a_j} - \frac{b_i}{\sum_{j=1}^{n}b_j}\right)\left(\log\left(\frac{a_i}{\sum_{j=1}^{n}a_j}\right) - \log\left(\frac{b_i}{\sum_{j=1}^{n}b_j}\right)\right) \tag{17}$$

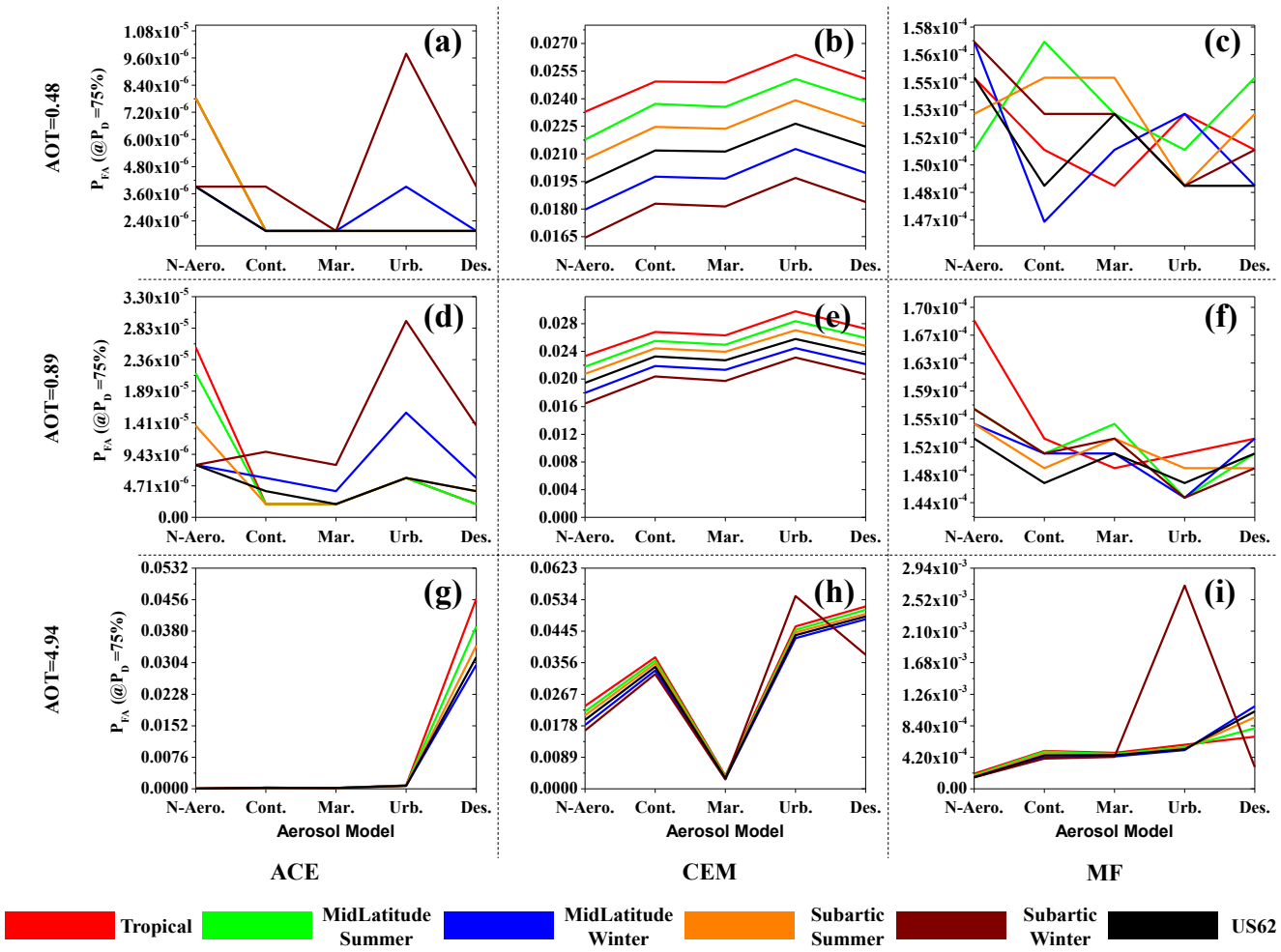

Fig. 14. Airborne imagery detection results. Illustrated are P_{FA} values when the $P_D = 75\%$ for the N1G target with simulated TOA target radiance spectra at (a-c) AOT = 0.48, (d-f) AOT = 0.89, and (g-i) AOT = 4.94 for different standard aerosol models (N-Aero. = No Aerosol, Cont. = Continental, Mar. = Maritime, Urb. = Urban, Des. = Desert) and atmospheric models (i.e., colored line) using the pixel-based THI target reflectance.

where D(**A**‖**B**) and D(**B**‖**A**) are called the relative entropy of **B** with respect to **A** and relative entropy of **A** with respect to **B**, respectively. Since SID is a probabilistic approach to measure the spectral similarity between two spectra, the SID score is an indication of the behavioral difference in the probability distribution function of any two pixels. A score close to zero from the SAM or SID indicates the spectra being compared are similar (Chang, 2003; van der Meer, 2006).

3. Results

In this section, we present the results of target detection for various TOA radiance spectra simulated under different atmospheric conditions. For ease of comparison of the performance by various algorithms, we benchmarked the P_{FA} for detection results at $P_D = 75\%$ for airborne image and $P_D = 50\%$ for space-borne imagery (Jha and Nidamanuri 2020). To illustrate this, we present an example (result for N1G by MF under various AOT conditions) in Fig. 6, showing the approach used to report results in this paper. We fixed the P_D at 75% (shown by the horizontal dotted line) and noted the first intersection point of the ROC curve and the $P_D = 75\%$ line to identify the respective P_{FA}.

3.1. Target detection performance from airborne imagery for simulated target spectra induced by AOT and atmospheric model assumption

3.1.1. Target detection performance under varying AOT conditions

This section presents the target detectability at various AOT values in the range 0–5 for two different input target reference sources, i.e., point and pixel mode with a tropical atmosphere and continental aerosol model.

3.1.1.1. Detection statistics for point-based field spectra. Fig. 7 shows the target detection performance by various target detectors for different target materials as a function of AOT. The input reference spectra were simulated using the point-based in-situ reflectance spectra. The influence of AOT on the detection performance is evident as the degree of detectability amongst the used algorithms varies significantly from one another and also differs from material to material of the targets used in the experiment. The robustness of detection due to the target spectra mismatch between reference and image spectra depends substantially on the AOT. As shown in Fig. 7, AOT's effect is profound after a certain threshold, such as after AOT = 2.5 in the case of N1G (Fig. 7(a)). The detection rate is least affected by the variation of AOT for the CEM detector. ACE, which detects materials based on spectral features (geometry-based), missed the target in most cases, even at low AOT values (higher visibility). For instance, for targets N2R, N3Y, and N4B, the P_{FA} is unusually high (0.35, 0.674, 0.39 at even low values of AOT). Moreover, in the cases where MF has detected targets unambiguously (e.g., for N1G, C1W), the change in AOT has resulted in a substantial increase in the number of FAs.

3.1.1.2. Detection statistics for pixel-based target spectra. Results of target

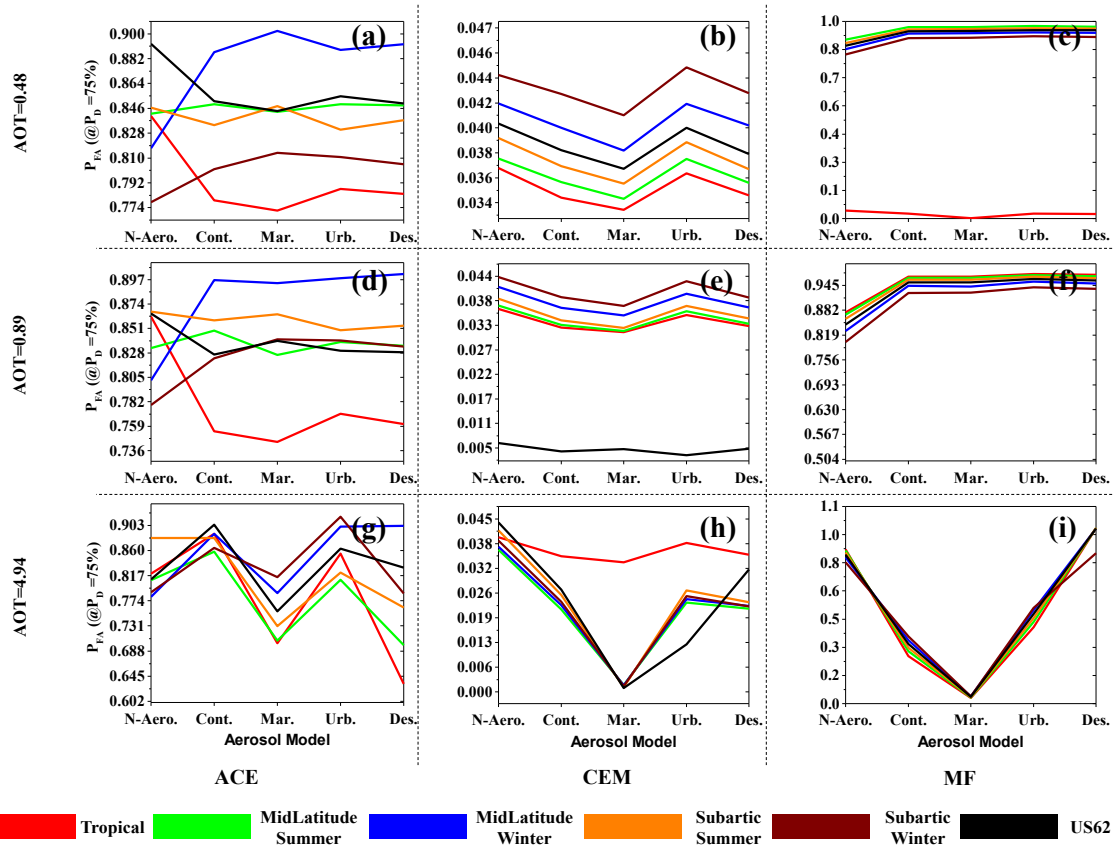

Fig. 15. Airborne imagery detection results. Illustrated are P_{FA} values when the $P_D = 75\%$ for the N4B target with simulated TOA target radiance spectra at (a-c) AOT = 0.48, (d-f) AOT = 0.89, and (g-i) AOT = 4.94 for different standard aerosol models (N-Aero. = No Aerosol, Cont. = Continental, Mar. = Maritime, Urb. = Urban, Des. = Desert) and atmospheric models (i.e., colored line) using the pixel-based THI target reflectance.

detection when spectra from THI were used as the input reference spectra are shown in Fig. 8. The input reference spectra were simulated from the THI based on reflectance spectra. In general, target detectability in airborne imagery using THI-based reference spectra in the radiance domain seems to have been substantially influenced by target contrast and background components (i.e., we see a variation with all materials, even at lower AOT's). It is evident from Fig. 8 that although N1G and N2R are satisfactorily detected by all three algorithms ($P_{FA} \sim 10^{-2} - 10^{-3}$), we might conclude that the MF and ACE detectors failed to detect the N3Y and N4B due to the high number of FAs. The failure of ACE and the MF, which are sensitive to the shape of spectral signature (Eismann, 2012), can be attributed to a mismatch of the simulated spectra and image spectra. In the case where successful detection of targets is possible, algorithms are almost impervious to change of AOT value up to 2.5.

3.1.2. Target detection performance as a function of standard aerosol models for different standard atmospheric models at various AOT values

In this section, we analyze the effects of varying the aerosol model (e.g., continental, maritime, etc.) within a given atmospheric model (e.g., tropical, US62, etc.) at different levels of AOT. Similar to Section 3.1.1, we present the results for both point and pixel-based target reference sources.

3.1.2.1. Detection statistics for point-based field spectra. Figs. 9 to 13 show the target detection performance of different detectors for the N1G (Fig. 9), N2R (Fig. 10), C1W (Fig. 11), N3Y (Fig. 12), and N4B (Fig. 13) targets. Detection results indicate inherent randomness in the performance. The performance is heavily penalized when choosing the "wrong" atmospheric model compared to a mismatch related to the aerosol model. For a lower AOT value (0.48 and 0.89), we see the aerosol models' influence at a given atmospheric model is not significant. However, at a high AOT value, the stability of detection performance reduces to a purely random phenomenon. Generally, for most of the targets such as N2R, N3Y, and N4B, the performance of the ACE detector is poor since the number of false alarms (FAs) for detection at $P_D = 75\%$ is staggeringly high, possibly caused by the sensitivity of the ACE detector to the spectral variability introduced in the reference target signal by the TOA radiance signal simulation process. MF and CEM are least affected by the aerosol model's variation, albeit different atmospheric models yielding different results. A tropical atmospheric model produces the best results for the MF detector, whereas CEM performs best for the Subarctic winter atmospheric model. We observe that the MF yields the best detection results ($P_{FA} \sim 10^{-4}$) for a particular atmospheric model (Tropical), but at the same time is very sensitive to changes in an atmospheric model (FAs amplify to 10–100 times). Although CEM yields inferior results compared to the MF for some of the targets (FAs in the range of $10^{-2} \sim 10^{-3}$ for N1G, C1W), the general takeaway is that the results are relatively stable and robust across various atmospheric models. This can be attributed to the nature of the MF detector, which is more sensitive to spectra shape in contrast to CEM, which can discriminate targets based on signal contrast of targets and background.

3.1.2.2. Detection statistics for pixel-based target spectra. We present selected results for the targets whose detection rate is either relatively the best or worst for brevity. Detection results for the N1G target in the THI-based in-situ spectrum show the best detectability among all the targets, as shown in Fig. 14, while the N4B target has the lowest detection rate. Although the choice of atmospheric model and aerosol

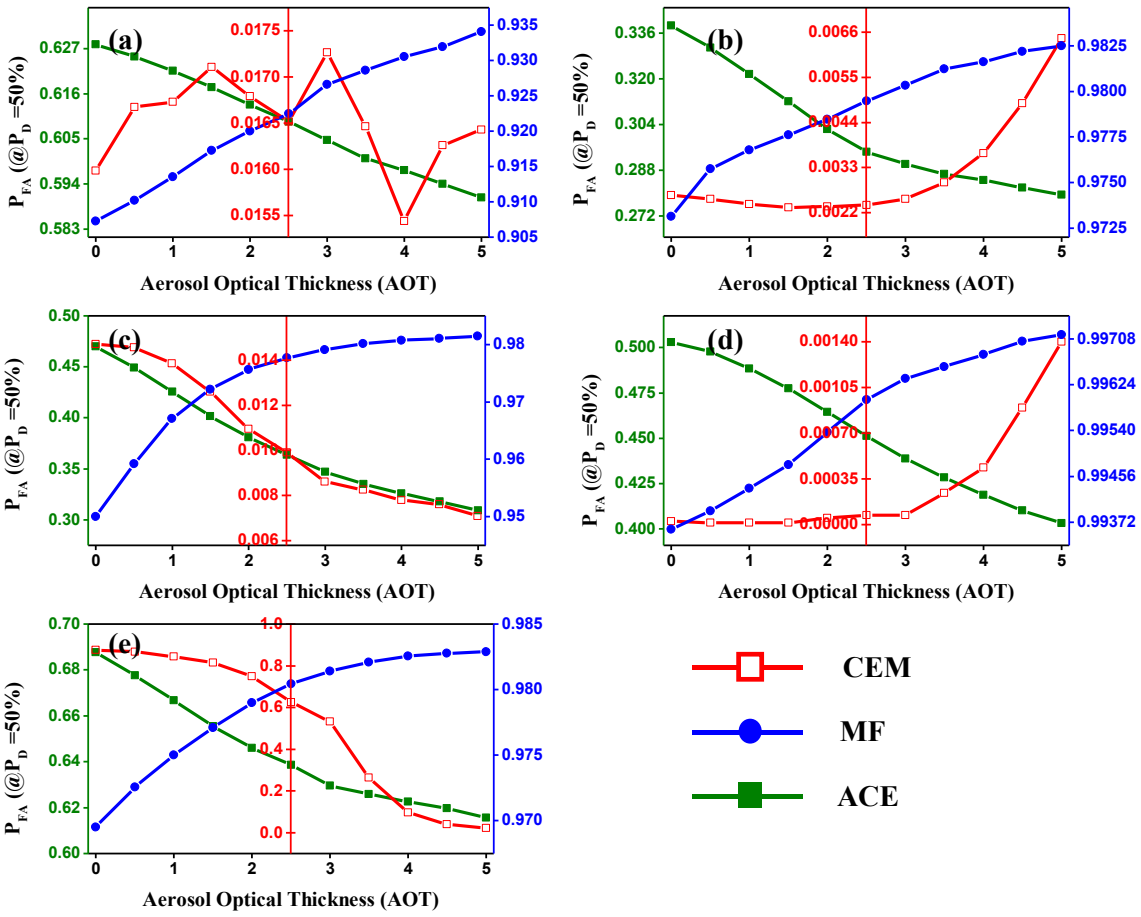

Fig. 16. Space-borne imagery detection results. Illustrated are P_{FA} values when the P_D = 50% for the targets (a) N1G, (b) N2R, (c) C1W, (d) N3Y, and (e) N4B with simulated TOA target radiance spectra at different AOT values between 0 and 5 using the point-based target reflectance.

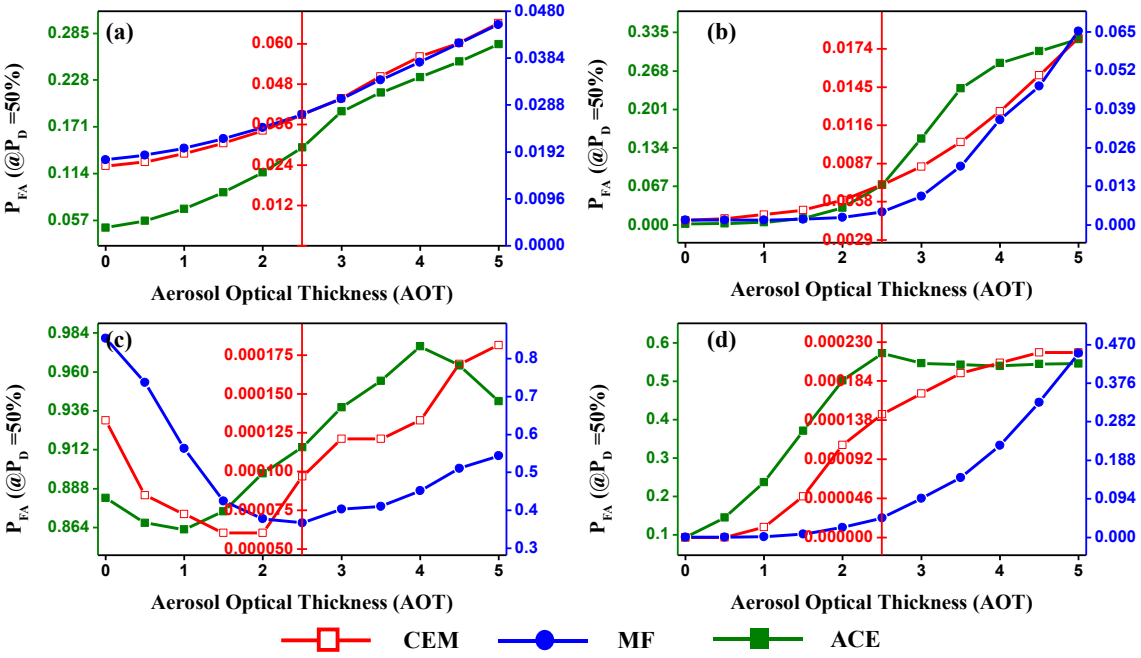

Fig. 17. Space-borne imagery detection results. Illustrated are P_{FA} values when the P_D = 50% for the targets (a) N1G, (b) N2R, (c) N3Y, and (d) N4B with simulated TOA target radiance spectra at different AOT values between 0 and 5 using the pixel-based THI target reflectance.

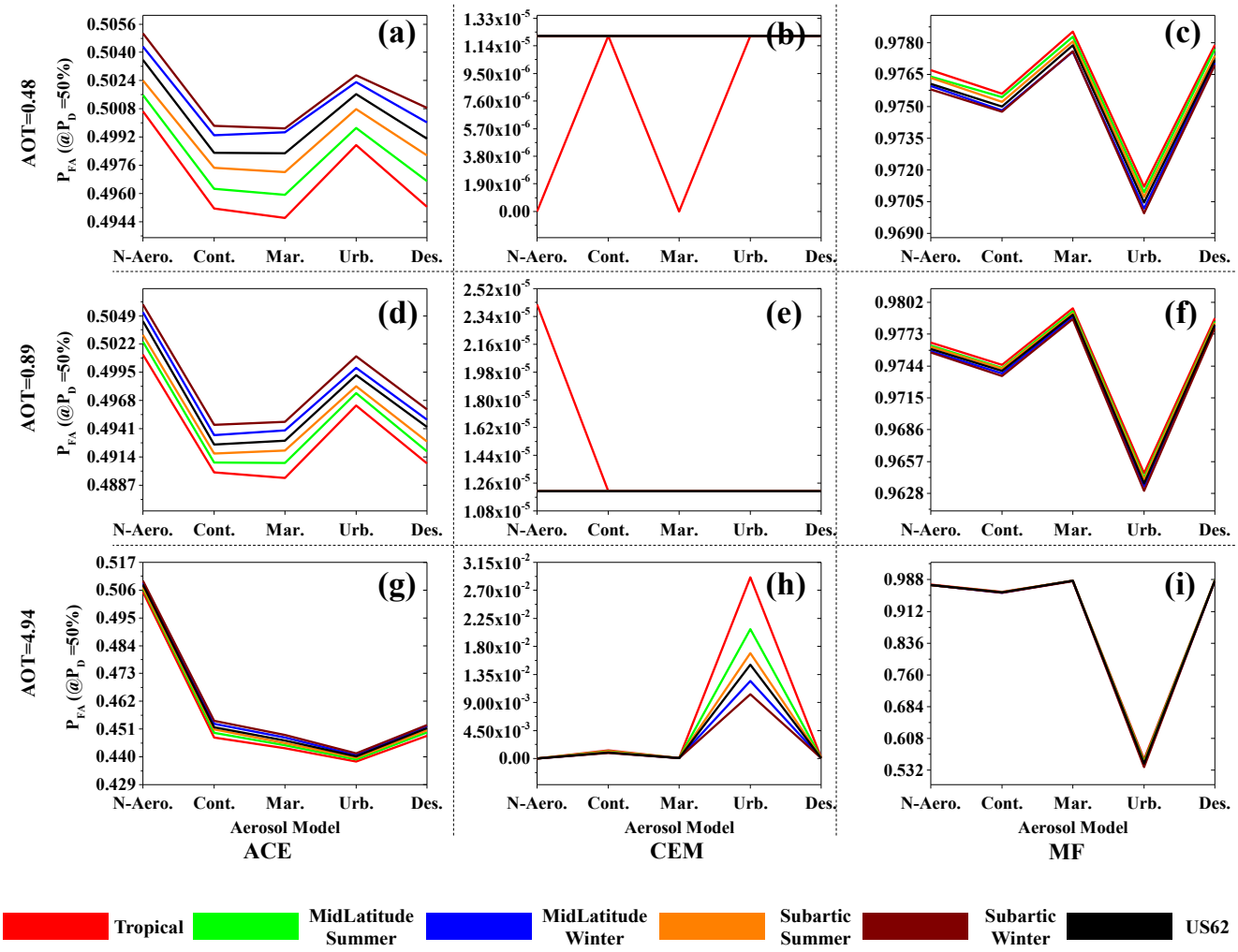

Fig. 18. Space-borne imagery detection results. Illustrated are P_{FA} values when the $P_D = 50\%$ for the N3Y target with simulated TOA target radiance spectra at (a-c) AOT = 0.48, (d-f) AOT = 0.89, and (g-i) AOT = 4.94 for different standard aerosol models (N-Aero. = No Aerosol, Cont. = Continental, Mar. = Maritime, Urb. = Urban, Des. = Desert) and atmospheric models (i.e., colored line) using the point-based target reflectance.

model at different AOT values does play a role in the levels of P_D and P_{FA}, the overall FA rate for N1G remains low regardless of the choice of different aerosol and atmospheric models. Among the ACE, CEM, and MF detectors, the lowest P_{FA} is obtained using ACE with an order of 10^{-5} –10^{-6} followed by MF with a FA rate at 10^{-4}. However, with a higher degree of AOT level (AOT = 4.94), ACE's performance takes a significant hit and the P_{FA} increases approximately 100 times to a level of 10^{-4}. On the other hand, although CEM's P_{FA} is highest amongst all the detection algorithms for the N1G target, the detection rate remains stable for different changes in aerosol and atmospheric models at several values of AOT, suggesting the robust nature of the detector.

In Fig. 15, we see that the performance levels for both ACE and MF change from a high detectability rate for N1G (Fig. 13) to complete failure for the case of N4B (Fig. 14). As observed for the case of point-based in-situ target spectra, spectral detectors like ACE and MF fail to detect most of the targets, whereas the CEM delivers a $P_{FA} \sim 10^{-3}$ for a tropical atmospheric model and a maritime aerosol model at all AOT levels.

3.2. Spectral target detection from space-borne imagery for simulated target spectra induced by AOT and atmospheric model assumption

3.2.1. Target detection performance under varying AOT conditions

3.2.1.1. Detection statistics for point-based field spectra. Fig. 16 shows the detection performance from space-borne imagery (Sentinel-2) using various detectors for all the simulated (i.e., different AOT values) target TOA radiance spectra derived from the field-based point reference spectra. Unlike the airborne sensor, the detectability of targets seems to be substantially influenced by the choice of AOT. The spectral variability caused by different AOT values plays an important role in detection. While the target detectors such as ACE and MF fail to detect all the targets, the CEM detector delivers an overall satisfactory performance with FAs in the range of $10^{-2} \sim 10^{-4}$. In particular, detection of N1G by CEM shows a highly random nature of detection using TOA radiance spectra. In contrast, successful detection of N2R, C1W (albeit high FA than N2R), and N3Y indicate the possibility of target detection from a space-borne platform. Missed targets such as N4B indicate the limited use of the space-borne remote imagery to detect dark materials, i.e., materials with low spectral radiant intensity for a point-based target reference.

3.2.1.2. Detection statistics for pixel-based THI spectra. Results of target

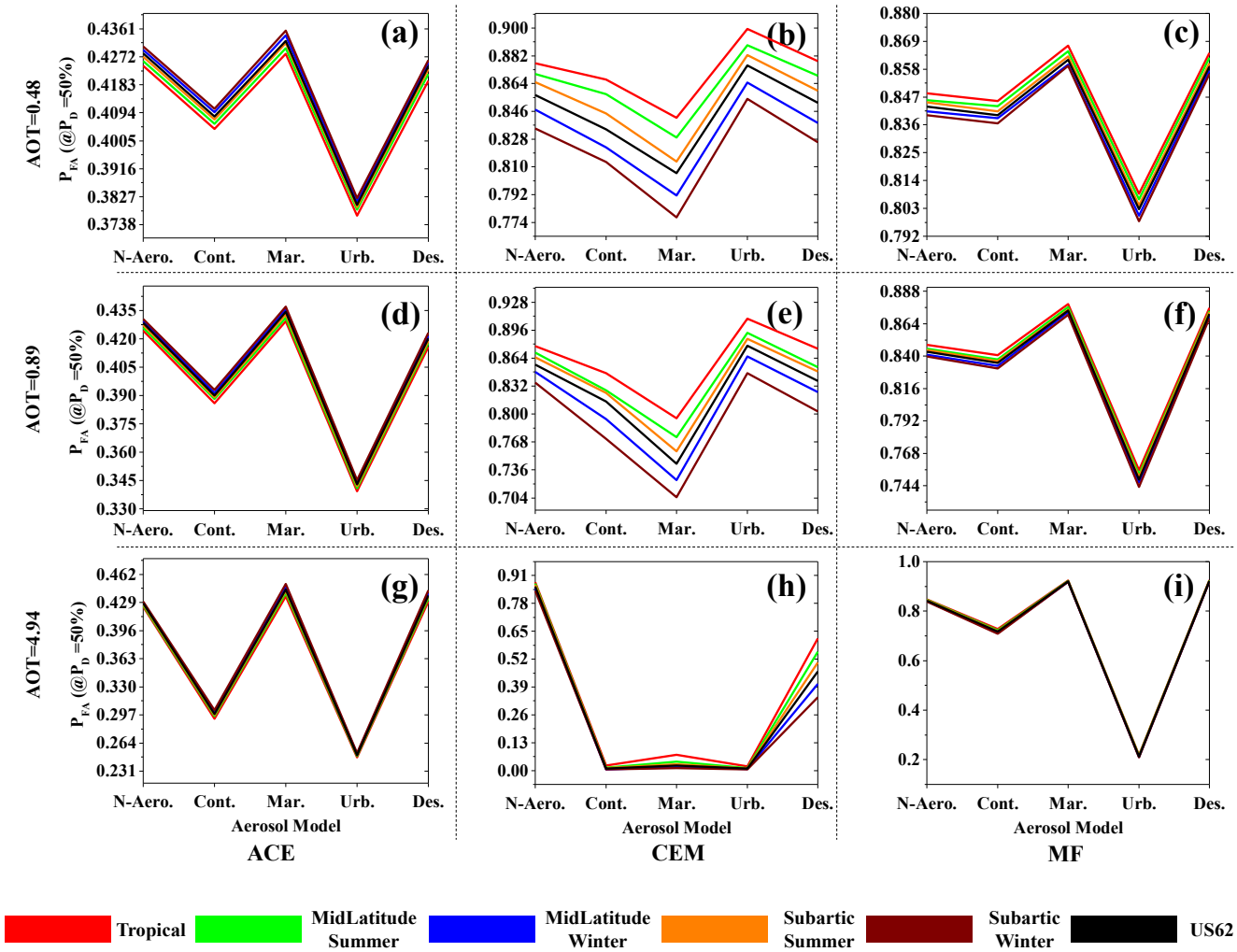

Fig. 19. Space-borne imagery detection results. Illustrated are P_{FA} values when the P_D = 50% for the N4B target with simulated TOA target radiance spectra at (a-c) AOT = 0.48, (d-f) AOT = 0.89, and (g-i) AOT = 4.94 for different standard aerosol models (N-Aero. = No Aerosol, Cont. = Continental, Mar. = Maritime, Urb. = Urban, Des. = Desert) and atmospheric models (i.e., colored line) using the point-based target reflectance.

detection in the space-borne imagery, when using the pixel-based THI spectra as reference target spectra, are shown in Fig. 17. The influence of AOT on detection performance is evident for most of the targets. We observe a pattern of performance degradation with increasing AOT for all the detectors across all the target materials. Unlike the previously observed low detection using point-based reference spectra for different AOT values, we now observe improved detection results using the pixel-based THI reference target spectra with lower FAs. Except for N3Y, all the detectors detect the targets with an acceptable P_{FA} ($10^{-2} \sim 10^{-6}$) at lower values (e.g., in the range 0 – 1) of the AOT, a clear advantage of pixel-based THI spectra over point-based spectra. Specifically, for targets N1G and N2R, there is a gradual change in detectability performance with AOT variation. In the case of N1G, FAs are low $(10^{-2} \sim 10^{-3})$ for AOT $\leq$ 0.5; while for N2R, there is minimal performance degradation on changing AOT until 2.5, and all the three detectors detected both the targets. Detection of N4B by the MF and CEM at a low FA ($P_{FA} = 0 \sim 10^{-5}$, although for AOT $\leq$ 1.5) is encouraging. In contrast to the apparent poor detection of a dark target (Section 3.2.1.1), while using the point-based in-situ target spectra, detection results from the pixel-based THI target reference spectra are comparatively superior. This suggests that the acquisition of ground target reference spectra using an imaging spectroradiometer is a better alternative over the general point-based spectroradiometer, especially in difficult and inaccessible terrain conditions.

3.2.2. *Target detection performance as a function of standard aerosol models for different standard atmospheric models at various AOT values*

3.2.2.1. Detection statistics for point-based field spectra. We present the best-case detection performance scenario in Fig. 18 and the worst-case scenario, where all the targets are missed, in Fig. 19. As observed in Section 1.2.1.1, the detection of targets using the FM approach from a space-borne platform for point-based in-situ target reference remains a challenge.

For N3Y, CEM's performance is satisfactory (Fig. 18(b-h)), and at a lower value of AOT (0.48 and 0.89), no significant impact related to atmospheric-aerosol models is observed. However, at AOT = 4.94 (Fig. 18(h)), we observe that, for all the atmospheric profiles, aerosol models such as continental, desert, and maritime yield a low number of FAs. In contrast, for the urban aerosol model, FAs depend upon the atmospheric profiles. Since most of the targets are not detectable by ACE and MF (high FA rate), the analysis of patterns in the FAs for different combinations of atmospheric conditions and aerosol models becomes trivial.

3.2.2.2. Detection statistics for pixel-based THI spectra. We now present the best-case scenario related to detection performance, as seen in Fig. 20 (observed for N2R), while the worst-case scenario, where the detectors miss N3Y, is shown in Fig. 21. A combination of the AOT

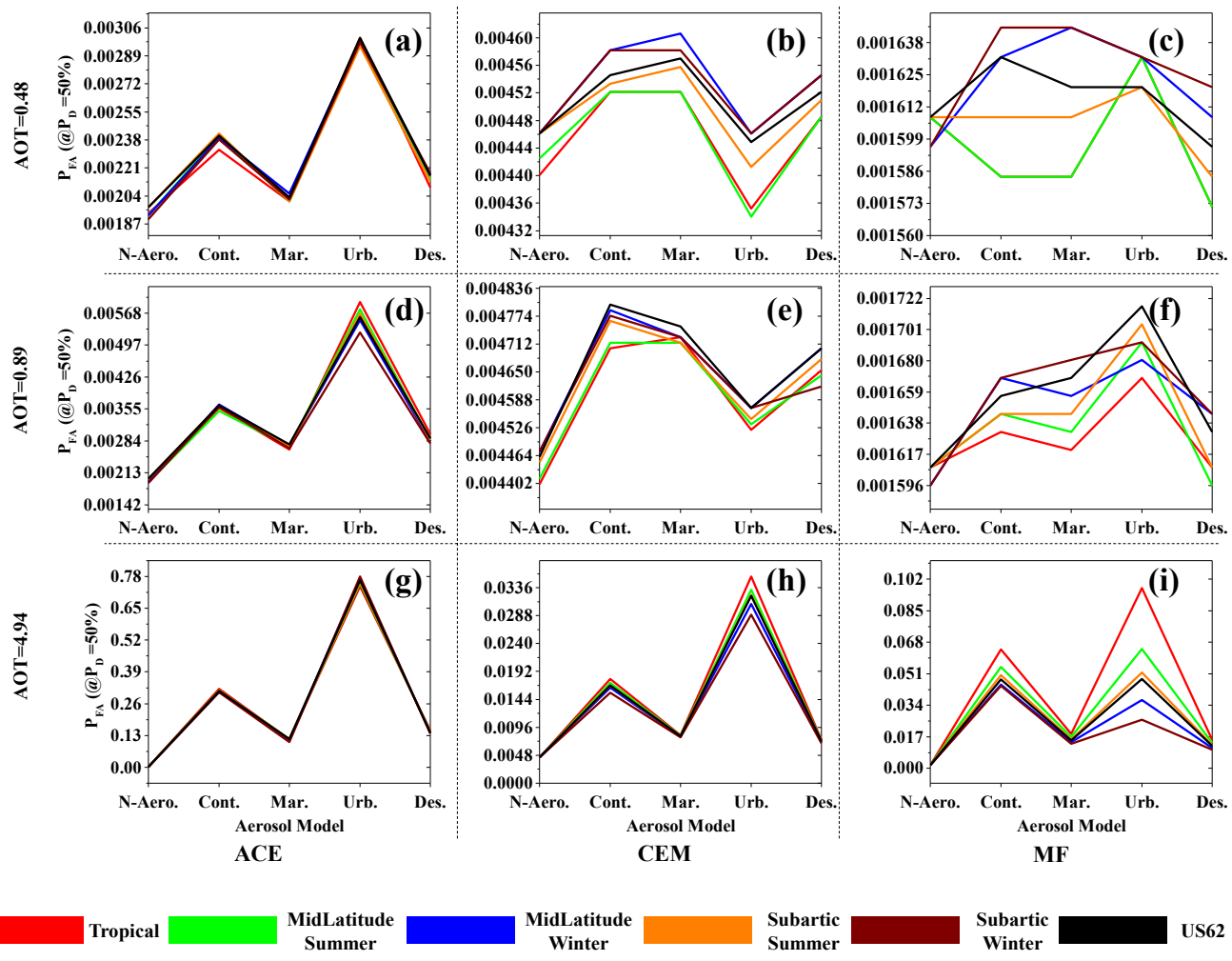

Fig. 20. Space-borne imagery detection results. Illustrated are P_{FA} values when the P_D = 50% for the N2R target with simulated TOA target radiance spectra at (a-c) AOT = 0.48, (d-f) AOT = 0.89, and (g-i) AOT = 4.94 for different standard aerosol models (N-Aero. = No Aerosol, Cont. = Continental, Mar. = Maritime, Urb. = Urban, Des. = Desert) and atmospheric models (i.e., colored line) using the pixel-based THI target spectra.

values, aerosol models, and atmospheric models plays a crucial role in determining target detectors' performance for a pixel-based input reference. As observed in Fig. 20, although all the target detectors detected N2R at lower AOT values with $P_{FA} \sim 10^{-3}$, the impact of aerosol models is evident. For instance, in the case of N2R detection by ACE (Fig. 20(a)), the performance degradation between maritime aerosol and urban aerosol model is 50%. Also, at AOT = 4.94, detection is most difficult by all detectors. Interestingly, for AOT $\leq$ 0.89, the pattern of FA increase and decrease is almost identical for each detector. As observed in previous sections, CEM is least affected by choice of aerosol models (~5–10% increase of FAs), whereas other spectral detectors such as ACE and MF are substantially affected. As observed for the case of point-based target reference, detection of N3Y using radiance spectra with the FM approach did not yield a better result, especially for the ACE and MF detectors.

3.3. Quantitative spectral similarity analysis of simulated and image spectra

The spectral similarity analysis between the target image spectrum from airborne imagery and the respective point-based in-situ reference spectrum is presented in Fig. 22 and Fig. 23. The results provided in this section are limited to the airborne imagery with AOT = 0.48 and 0.89, as sufficient inferences can be drawn about the underlying physical state of the atmospheric conditions. These observations and findings can be generalized for other cases as well.

As observed in Fig. 22 and Fig. 23, we can identify the atmospheric conditions i.e., probable aerosol models (i.e., colored lines) for a given atmospheric profile which would yield successful detection results in unknown atmospheric conditions. For example, we find the Tropical and Midlatitude Summer atmospheric profile in the present experimental setup, with either the Continental or Maritime aerosol model, the best suited for the given experimental site. As observed from the results in Section 3.1.2, indeed, the Tropical atmospheric profile with the Continental aerosol model does provide better results compared to other combinations of models. Furthermore, we find the spectral matching different across the targets, suggesting that there is an effect related to the spatial neighborhood, which is separate from parameters related to the atmosphere.

4. Discussion

Onboard methods for problems ranging from classification, anomaly detection, unmixing to target detection, etc., are projected to be future endeavors in the field of remote sensing. FM approach helps to design an onboard computational framework for realizing remote sensing-based real-time target detection system. Spectral target detection by its nature involves sparsely populated pixels of the imagery, which increases the chance of a target miss with even a slight miscalculation of atmospheric parameters. Few seminal studies on target detection have shown

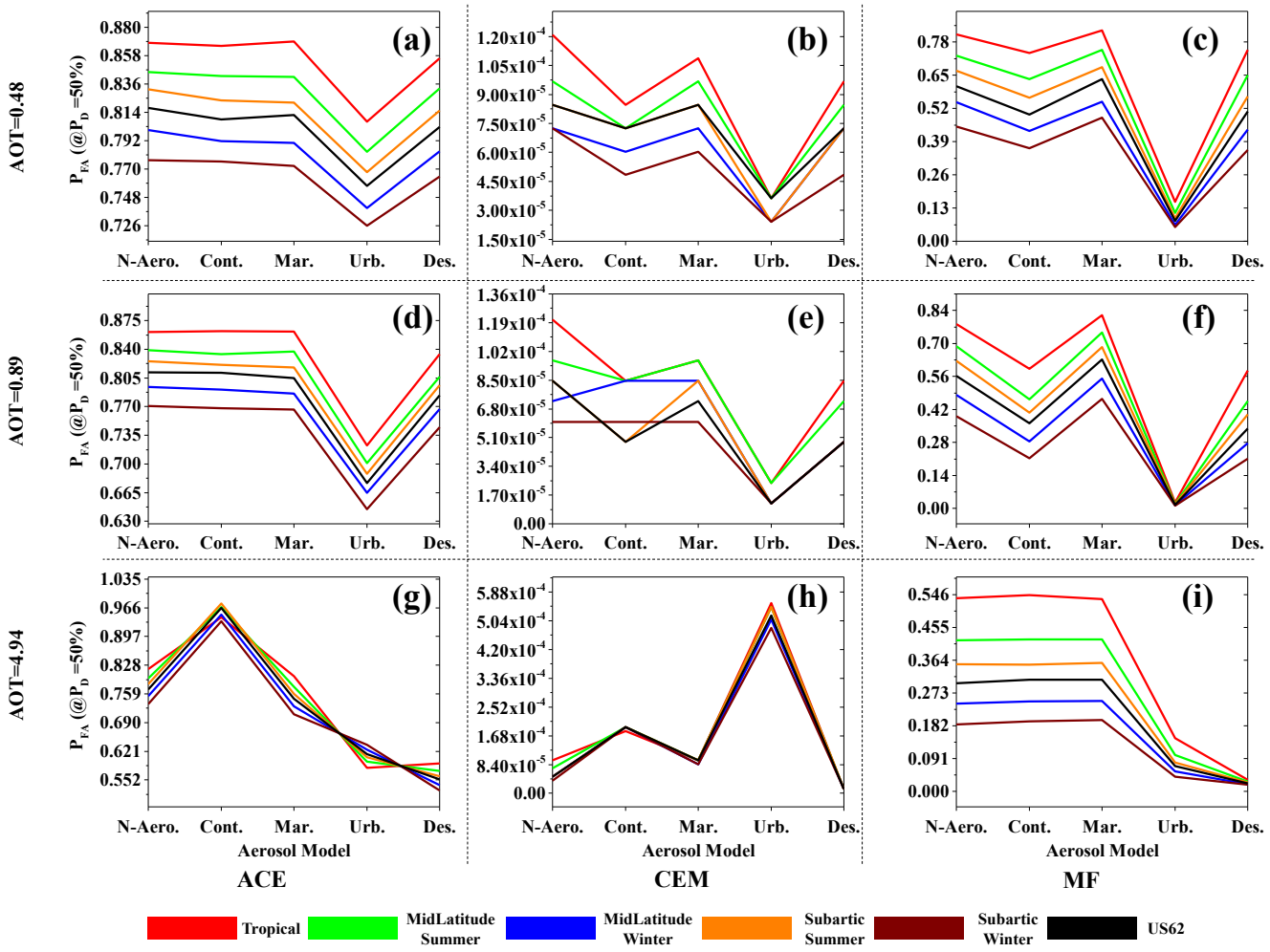

Fig. 21. Space-borne imagery detection results. Illustrated are P_{FA} values when the P_D = 50% for the N3Y target with simulated TOA target radiance spectra at (a-c) AOT = 0.48, (d-f) AOT = 0.89, and (g-i) AOT = 4.94 for different standard aerosol models (N-Aero. = No Aerosol, Cont. = Continental, Mar. = Maritime, Urb. = Urban, Des. = Desert) and atmospheric models (i.e., colored line) using the pixel-based THI target spectra.

the FM approach as a potential solution for a computationally efficient framework (Ientilucci and Bajorski, 2010; Acito et al., 2015), although the effect of atmospheric variables on detection performance has not been taken into account. In this paper, we have presented the FM approach to account for atmosphere-induced target uncertainty and variability in multi-platform target detection data, which to the best of our knowledge, has not been reported in the literature. We have also presented results from a hypothetical perspective where the spectral knowledge of a target in one given space–time frame can be transferred for detection in a different space–time framework. This involves two different sets of atmospheric components, and as a result, a mismatch of atmospheric parameters may hamper the detectability of the target. The findings in this research could be used for drawing important inferences and gain a comprehensive insight into the extent and nature of the atmosphere influences and impacts of parameter mismatch, which ultimately affects target detection performance.

4.1. Influence of spectral variation caused by varying AOT on detection performance

AOT, which corresponds to columnar visibility, is one of the key atmospheric variables that impact the sensor reaching radiance. Several studies have established the uncertainty caused by AOT while estimating biophysical parameters (Gillingham et al., 2013; Marcello et al., 2016). Most of the reported studies are focused on objects covering a large portion of the image (a class such as vegetation or forest). Since AOT is sensitive to wavelength, absorption feature, surface albedo (Bhatia et al., 2015), and pixel to pixel differences in AOT levels (Wilson et al., 2014), it is natural to expect that these effects would be reflected in target detection performance.

For the most efficient target detector (CEM), examining the detection from airborne imagery (i.e., Fig. 7, Section 3.1.1.1) for the point-based in-situ target reference, the overall variation in detection performance is 2% − 15% across all the targets for the simulated spectra at AOTs ≤ 2.5. For spectral detectors, MF and ACE, where the targets can be deemed as detected (with lower FAs), the variation in detection range is between 10% − 90% for most of the targets. A similar trend is observed from space-borne imagery for the point-based in-situ target reference. However, for the pixel-based target reference, the detection from airborne imagery shows substantial variation with AOT levels (e.g., ACE for N1G varied by 200% with AOT ≤ 2.5). The variation is linear with a change in AOT levels for detection from space-borne imagery using the pixel-based target reference.

Overall, detection performance and the FAs are found to vary moderately across all the targets, albeit with different scales. Results indicate that the AOT mismatch effect yields different detection results for targets having different surface properties. Although the given targets in this experiment vary predominantly only in the visible portion of the EM spectrum, the varying effects of AOT mismatch across the targets suggest an involvement related to the background pixels and an AOT

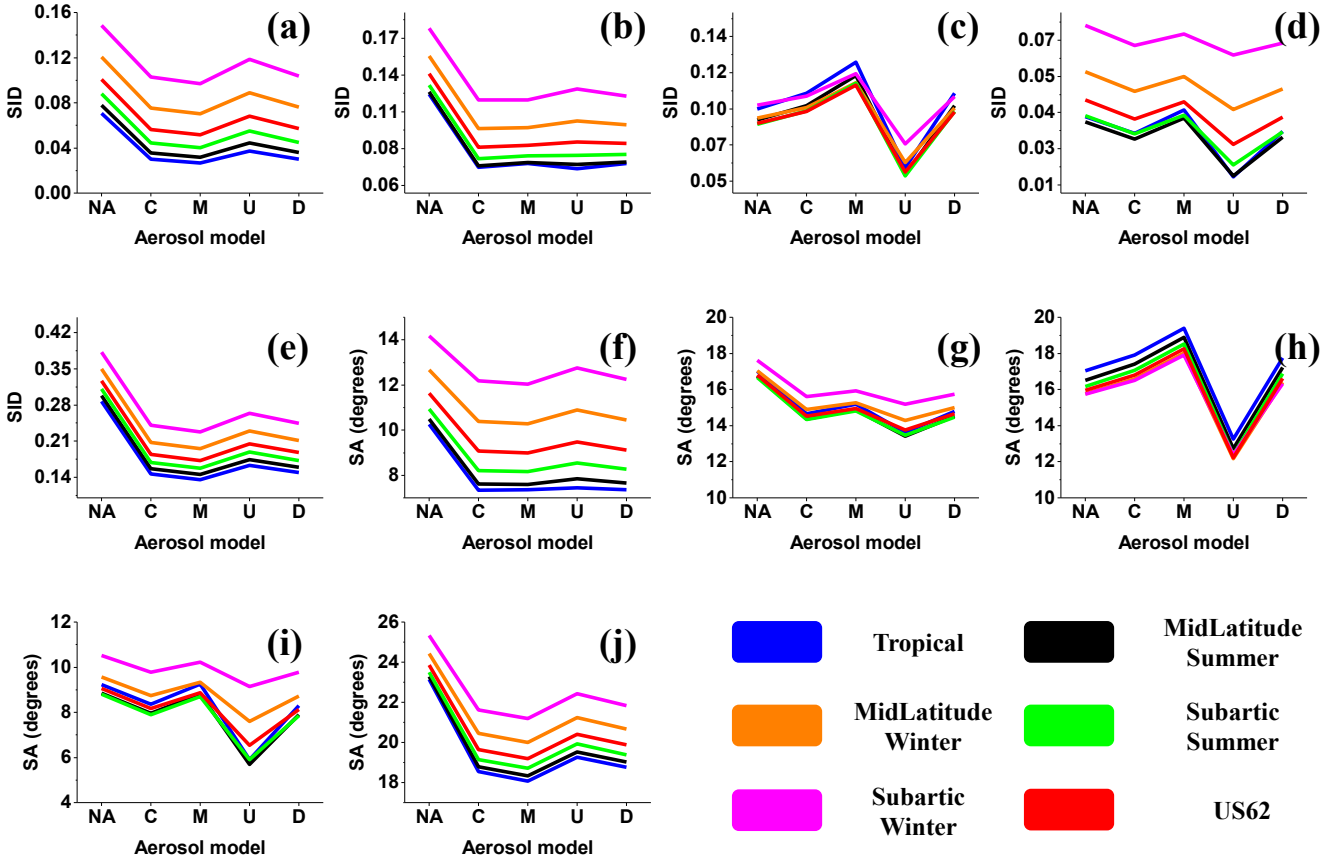

Fig. 22. Spectral similarity score for the point-based in-situ target reference target spectra and the corresponding image spectra for (a, f, k, p) N1G, (b, g, l, q) N2R, (c, h, m, r) C1W, (d, i, n, s) N3Y, and (e, j, o, t) N4B targets at AOT = 0.48 for different atmospheric (i.e., colored line) and aerosol models (NA = No Aerosol, C = Continental, M = Maritime, U = Urban, D = Desert).

influence which seems to impact overall detection performance.

4.2. Influence of atmospheric model and respective mismatch on target detection performance

Apart from the AOT, the other two critical parameters seen in several RTM are the choice of atmospheric and aerosol models. Typically, atmospheric models in 6S are modeled on the basis of fixed columnar profiles, which are pre-computed using standard models such as that by Goody and Yung (1995), Malkmus (1967), and McClatchey et al. (1971) for estimating gaseous transmittance, columnar water vapor, temperature, pressure, and ozone concentrations as a function of altitude. Similarly, aerosol models are formulated based on the models of Lenoble (1985), D'Almeida et al. (1991). These models estimate the macroscopic properties of EM signal propagation in the atmosphere. For these reasons, they are often treated like a "black box" (Bhatia, 2018). However, since these global models are widely used in remote sensing for atmospheric compensation and represent the atmospheric state in a given space–time, we have investigated their impact on target detection. Detection results from airborne imagery using the point-based in-situ target reference indicate that the overall detection and levels of FAs are predominantly determined by the choice of atmospheric profile. A mismatch of atmospheric profile can potentially lead to detection failure. We have noticed that for a given atmospheric profile (e.g., Tropical), there is an observable pattern related to the aerosol models on the number of FAs, which indicates the need for estimation of local aerosol models in all automated target detection frameworks. Interestingly, spectral target detectors such as ACE and MF have yielded low FAs for a tropical atmospheric profile. In contrast, the CEM detector offers a better result for the Subarctic winter atmospheric profile. This insinuates that the target detection results can be different across various detection algorithms for different atmospheric state variables.

We suggest that a detection framework for applications utilizing the FM approach for target detection must be designed keeping in mind the nature of the detection algorithm and its sensitivity to atmospheric state variables. Target detection in airborne imagery using pixel-based target reference spectra indicates that the detection of dark targets (i.e., targets with lower reflection intensity) is a challenge and is influenced by the choice of atmospheric parameters. On the other hand, although the detection is low for space-borne imagery using both the point-based and pixel-based target references, the pattern observed in the levels of FAs is concurrent with the observations in Section 3.1.2 for the ACE and MF target detectors.

The target detection algorithms used in this work were chosen from the perspective of onboard spectral target detection and the FM approach. However, the target detection in hyperspectral imagery, especially in offline mode, can benefit from using other evolving methods such as kernel-based and deep machine learning methods. We recommend studies emphasizing this aspect from both the reflectance and radiance modes of target detection.

5. Conclusion

Spectral target detection is a critical application of hyperspectral remote sensing. There have been considerable efforts to develop signal processing-based detection algorithms in this field. However, to a lesser degree, the underlying physical phenomena have largely been overlooked. The trivialization of the electromagnetic signal propagation model, ignoring the subtle atmospheric process, can produce ambiguous detection results. This study has attempted the quantitative assessment

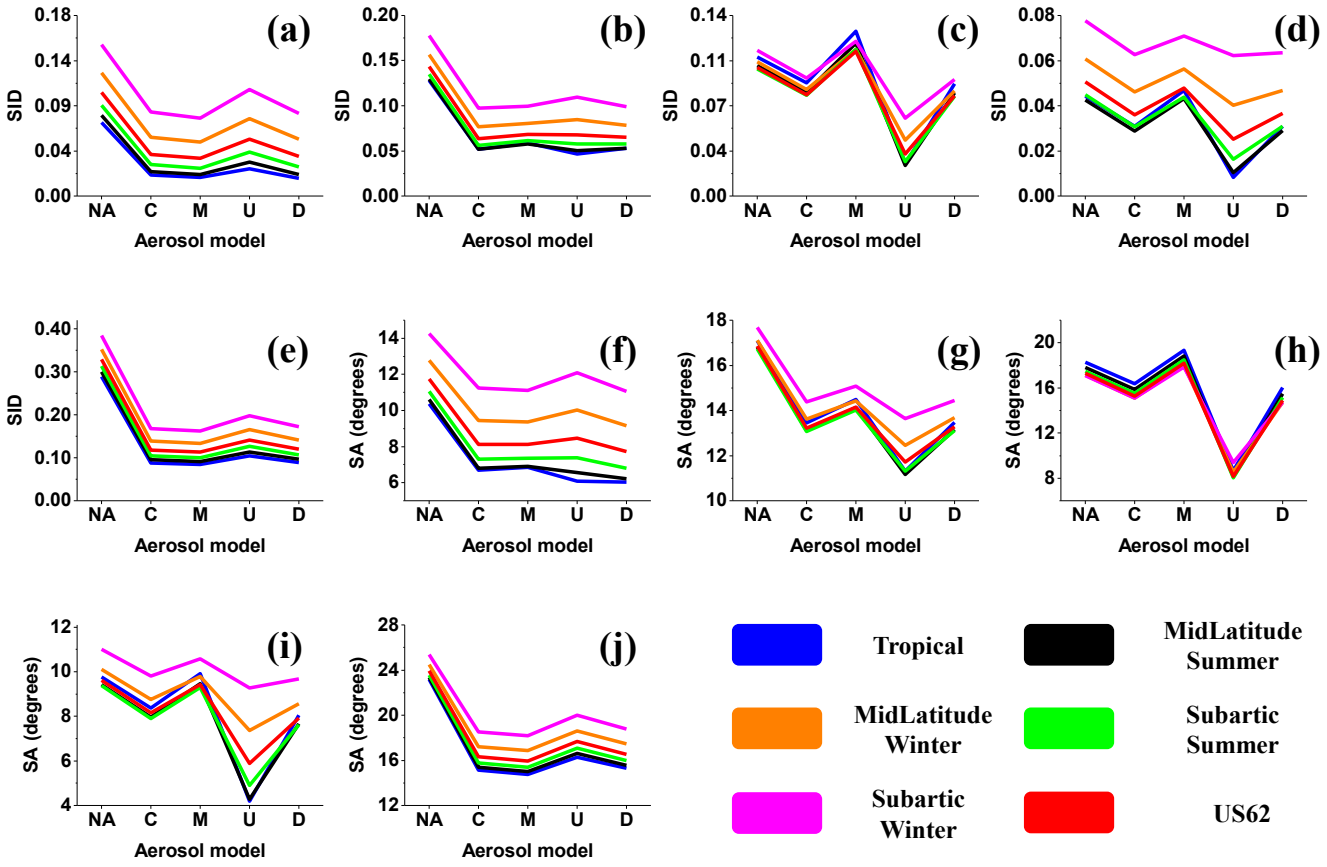

Fig. 23. Spectral similarity score for the point-based in-situ target reference target spectra and the corresponding image spectra for (a, f, k, p) N1G, (b, g, l, q) N2R, (c, h, m, r) C1W, (d, i, n, s) N3Y, and (e, j, o, t) N4B targets at AOT = 0.89 for different atmospheric(i.e., colored line) and aerosol models (NA = No Aerosol, C = Continental, M = Maritime, U = Urban, D = Desert).

of hyperspectral target detection from a radiative transfer perspective and has extended the FM approach for target detection to a multi-platform (airborne - space-borne) target detection setup. Given that the FM approach is computationally inexpensive, we recommend the FM approach for all kinds of onboard processing methods for detecting non-critical targets (i.e., environmental pollution surveillance, infrastructure build-up in strategic areas, unauthorized construction in protected forest areas, geochemical exploration, mineral prospecting, etc.). From an atmospheric parameter modeling perspective, spectral target detection is susceptible to AOT, atmospheric profile, and aerosol model. AOT is found to be the most dominant factor among the parameters considered, having substantial implications on the detectability of targets. At a given AOT, the choice of atmospheric and aerosol profiles has a bearing on the levels of FAs. The wrong choice of atmospheric models can lead to a high rate of FAs. The variations in target detection due to AOT can be reduced to a moderate degree by choosing an appropriate detection algorithm (e.g., CEM for the present application). The validity of the hypothesis that targets can be detected by transferring target spectral knowledge from a known atmospheric state to an unknown state is case-specific. The lack of a priori knowledge on the exact atmospheric condition can limit the target detection process. Tackling such problems requires a learning approach to model the targets that account for the atmospheric processes' induced spectral variability.

Two significant findings from the research, apart from the atmospheric perspective on target detection, are establishing the efficacy of the pixel-based in-situ target reference and the potential of detection of engineered targets from space-borne platforms. The ground-based imaging spectroscopy-derived target reference spectra perform well with detection from space-borne imagery. The FM approach for space-borne imagery produced unambiguous detection results for several targets indicating a strong potential for developing automatic satellite-based spectral target detection frameworks. We believe that more experimental datasets and additional testing at different sites would enhance our understanding of the target detection process and its intricate relation to atmospheric influences.

Funding

This research was funded by the Department of Science and Technology, Government of India (Grant Number: BDID/01/23/2014-HSRS/37) as part of the Network Programme on Imaging Spectroscopy and Applications (NISA).

Declaration of Competing Interest

The authors declare that they have no known competing financial interests or personal relationships that could have appeared to influence the work reported in this paper.

Acknowledgments

The authors would like to thank the Space Application Centre (SAC) from India, and Jet Propulsion Lab (JPL), from the USA, for facilitating the airborne hyperspectral imagery acquired as part of the collaboration between ISRO, India, and NASA, USA. We acknowledge the European Space Agency (ESA) for providing the Sentinel-2 satellite imagery. We express our sincere gratitude to the anonymous reviewers for helping us with critical suggestions for improving the quality of our article.

References

Acito, N., Corsini, G., Diani, M., Matteoli, S., Riccobono, A., Rossi, A., 2015. Validation of forward modeling target detection approach on a new hyperspectral data set featuring an urban scenario and variable illumination conditions. In: in: 2015 IEEE International Geoscience and Remote Sensing Symposium (IGARSS). Presented at the 2015 IEEE International Geoscience and Remote Sensing Symposium (IGARSS), pp. 5075–5078. https://doi.org/10.1109/IGARSS.2015.7326974.

Agapiou, A., Hadjimitsis, D.G., Papoutsa, C., Alexakis, D.D., Papadavid, G., 2011. The Importance of Accounting for Atmospheric Effects in the Application of NDVI and Interpretation of Satellite Imagery Supporting Archaeological Research: The Case Studies of Palaepaphos and Nea Paphos Sites in Cyprus. Remote Sens. 3, 2605–2629. https://doi.org/10.3390/rs3122605.

Axelsson, M., Friman, O., Haavardsholm, T.V., Renhorn, I., 2016. Target detection in hyperspectral imagery using forward modeling and in-scene information. ISPRS J. Photogramm. Remote Sens. 119, 124–134.

Ayhan, B., Kwan, C., 2017. On the use of radiance domain for burn scar detection under varying atmospheric illumination conditions and viewing geometry. Signal Image Video Process. 11 (4), 605–612. https://doi.org/10.1007/s11760-016-1000-8.

Bhatia, N., 2018. Uncertainty Propagation of Atmospheric Correction Parameters. PhD Thesis, Faculty of Geo-Information Science and Earth Observation University of Twente, The Netherlands. https://doi.org/10.17026/dans-xjk-5sat.

Bhatia, N., Tolpekin, V.A., Reusen, I., Sterckx, S., Biesemans, J., Stein, A., 2015. Sensitivity of Reflectance to Water Vapor and Aerosol Optical Thickness. IEEE J. Sel. Top. Appl. Earth Obs. Remote Sens. 8 (6), 3199–3208. https://doi.org/10.1109/JSTARS.2015.2425954.

Bhatia, N., Tolpekin, V.A., Stein, A., Reusen, I., 2018. Estimation of AOD Under Uncertainty: An Approach for Hyperspectral Airborne Data. Remote Sens. 10, 947. https://doi.org/10.3390/rs10060947.

Bhattacharya, B.K., Green, R.O., Rao, S., Saxena, M., Sharma, S., Kumar, K.A., Srinivasulu, P., Sharma, S., Dhar, D., Bandyopadhyay, S., Bhatwadekar, S., 2019. An overview of AVIRIS-NG airborne hyperspectral science campaign over India. Curr. Sci. 116, 1082–1088.

Briottet, X., Boucher, Y., Dimmeler, A., Malaplate, A., Cini, A., Diani, M., Bekman, H.H.P. T., Schwering, P., Skauli, T., Kasen, I., Renhorn, I., 2006. Military applications of hyperspectral imagery, in: Targets and Backgrounds XII: Characterization and Representation. International Society for Optics and Photonics, p. 62390.

Bue, B.D., Thompson, D.R., Eastwood, M., Green, R.O., Gao, B.-C., Keymeulen, D., Sarture, C.M., Mazer, A.S., Luong, H.H., 2015. Real-Time Atmospheric Correction of AVIRIS-NG Imagery. IEEE Trans Geosci. Remote Sens. 53 (12), 6419–6428.

Chang, C.I., 2003. Hyperspectral imaging: techniques for spectral detection and classification. Springer Science & Business Media.

Chang, C.I., 2000. An information-theoretic approach to spectral variability, similarity, and discrimination for hyperspectral image analysis. IEEE Trans. Inf. Theory 46, 1927–1932.

Chen, S.-Y., Lin, C., Chuang, S.-J., Kao, Z.-Y., 2019. Weighted Background Suppression Target Detection Using Sparse Image Enhancement Technique for Newly Grown Tree Leaves. Remote Sens. 11 (9), 1081. https://doi.org/10.3390/rs11091081.

Cheng, G., Han, J., Lu, X., 2017. Remote Sensing Image Scene Classification: Benchmark and State of the Art. Proc. IEEE 105 (10), 1865–1883. https://doi.org/10.1109/JPROC.2017.2675998.

D'Almeida, G.A., Koepke, P., Shettle, E.P., 1991. Atmospheric aerosols: global climatology and radiative characteristics. A Deepak Pub.

Du, J., Li, Z., 2018. A Hyperspectral Target Detection Framework With Subtraction Pixel Pair Features. IEEE Access 6, 45562–45577. https://doi.org/10.1109/ACCESS.2018.2865963.

Eismann, M.T., 2012. Hyperspectral remote sensing. SPIE, Bellingham.

Field Spectroscopy Guide with SVC i-series Spectroradiometers, 2010.

Geng, X., Ji, L., Sun, K., 2016. Clever eye algorithm for target detection of remote sensing imagery. ISPRS J. Photogramm. Remote Sens. 114, 32–39. https://doi.org/10.1016/j.isprsjprs.2015.10.014.

Gillingham, S.S., Flood, N., Gill, T.K., 2013. On determining appropriate aerosol optical depth values for atmospheric correction of satellite imagery for biophysical parameter retrieval: Requirements and limitations under Australian conditions. Int. J. Remote Sens. 34 (6), 2089–2100.

Goody, R.M., Yung, Y.L., 1995. Atmospheric radiation: theoretical basis. Oxford University Press.

Gyaneshwar, D., Nidamanuri, R.R., 2020. A real-time FPGA accelerated stream processing for hyperspectral image classification. Geocarto Int. 1–18.

Hussain, M., Chen, D., Cheng, A., Wei, H., Stanley, D., 2013. Change detection from remotely sensed images: From pixel-based to object-based approaches. ISPRS J. Photogramm. Remote Sens. 80, 91–106. https://doi.org/10.1016/j.isprsjprs.2013.03.006.

Ientilucci, E.J., 2017. Spectral target detection considerations from a physical modeling perspective, in: 2017 IEEE International Geoscience and Remote Sensing Symposium (IGARSS). Presented at the 2017 IEEE International Geoscience and Remote Sensing Symposium (IGARSS), pp. 1320–1323. https://doi.org/10.1109/IGARSS.2017.8127204.

Ientilucci, E.J., Adler-Golden, S., 2019. Atmospheric Compensation of Hyperspectral Data: An Overview and Review of In-Scene and Physics-Based Approaches. IEEE Geosci. Remote Sens. Mag. 7 (2), 31–50. https://doi.org/10.1109/MGRS.2019.2904706.

Ientilucci, E.J., Bajorski, P., 2010. Hyperspectral target detection in a whitened space utilizing forward modeling concepts, in: 2010 2nd Workshop on Hyperspectral Image and Signal Processing: Evolution in Remote Sensing. Presented at the 2010 2nd Workshop on Hyperspectral Image and Signal Processing: Evolution in Remote Sensing, pp. 1–5. https://doi.org/10.1109/WHISPERS.2010.5594939.

Ientilucci, E.J., Bajorski, P., 2006. Statistical models for physically derived target subspaces, in: Shen, S.S., Lewis, P.E. (Eds.), Presented at the SPIE Optics + Photonics, San Diego, California, USA, p. 63020A. https://doi.org/10.1117/12.679525.

Jha, S.S., Kumar, M., Nidamanuri, R.R., 2020. Multi-platform optical remote sensing dataset for target detection. Data Brief 33, 106362. https://doi.org/10.1016/j.dib.2020.106362.

Jha, S.S., Nidamanuri, R.R., 2020. Gudalur Spectral Target Detection (GST-D): A New Benchmark Dataset and Engineered Material Target Detection in Multi-Platform Remote Sensing Data. Remote Sens. 12, 2145. https://doi.org/10.3390/rs12132145.

Kim, T.-S., Oh, S., Chun, T.B., Lee, M., 2019. Impact of Atmospheric Correction on the Ship Detection Using Airborne Hyperspectral Image, in: IGARSS 2019-2019 IEEE International Geoscience and Remote Sensing Symposium. IEEE, pp. 2190–2192.

Kruse, F.A., Lefkoff, A.B., Boardman, J.W., Heidebrecht, K.B., Shapiro, A.T., Barloon, P. J., Goetz, A.F.H., 1993. The spectral image processing system (SIPS)—interactive visualization and analysis of imaging spectrometer data. Remote Sens. Environ. 44 (2-3), 145–163.

Kwan, C., Gribben, D., Ayhan, B., Li, J., Bernabe, S., Plaza, A., 2020. An Accurate Vegetation and Non-Vegetation Differentiation Approach Based on Land Cover Classification. Remote Sens. 12, 3880. https://doi.org/10.3390/rs12233880.

Lenoble, J., 1985. Radiative transfer in scattering and absorbing atmospheres: standard computational procedures. A. Deepak Hampton, Va.

Louis, J., Debaecker, V., Pflug, B., Main-Knorn, M., Bieniarz, J., Mueller-Wilm, U., Cadau, E., Gascon, F., 2016. Sentinel-2 sen2cor: L2a processor for users, in: Proceedings Living Planet Symposium 2016. Spacebooks Online, pp. 1–8.

Lu, X., Zheng, X., Yuan, Y., 2017. Remote Sensing Scene Classification by Unsupervised Representation Learning. IEEE Trans. Geosci. Remote Sens. 55 (9), 5148–5157. https://doi.org/10.1109/TGRS.2017.2702596.

Malkmus, W., 1967. Random Lorentz band model with exponential-tailed S- 1 line-intensity distribution function. JOSA 57 (3), 323. https://doi.org/10.1364/JOSA.57.000323.

Manolakis, D., 2005. Taxonomy of detection algorithms for hyperspectral imaging applications. Opt. Eng. 44 (6), 066403. https://doi.org/10.1117/1.1930927.

Manolakis, D., Marden, D., Shaw, G.A., 2003. Hyperspectral image processing for automatic target detection applications. Linc. Lab. J. 14, 79–116.

Manolakis, D.G., Lockwood, R.B., Cooley, T.W., 2016. Hyperspectral imaging remote sensing: physics, sensors, and algorithms. Cambridge University Press.

Marcello, J., Eugenio, F., Perdomo, U., Medina, A., 2016. Assessment of Atmospheric Algorithms to Retrieve Vegetation in Natural Protected Areas Using Multispectral High Resolution Imagery. Sensors 16, 1624. https://doi.org/10.3390/s16101624.

Martins, V.S., Barbosa, C.C.F., De Carvalho, L.A.S., Jorge, D.S.F., Lobo, F. de L., Novo, E. M.L. de M., 2017. Assessment of atmospheric correction methods for Sentinel-2 MSI images applied to Amazon floodplain lakes. Remote Sens. 9, 322.

Matteoli, S., Ientilucci, E.J., Kerekes, J.P., 2011. Operational and performance considerations of radiative-transfer modeling in hyperspectral target detection. IEEE Trans. Geosci. Remote Sens. 49 (4), 1343–1355.

Matteoli, S., Ientilucci, E.J., Kerekes, J.P., 2009. Forward Modeling and Atmospheric Compensation in hyperspectral data: Experimental analysis from a target detection perspective, in: 2009 First Workshop on Hyperspectral Image and Signal Processing: Evolution in Remote Sensing. Presented at the 2009 First Workshop on Hyperspectral Image and Signal Processing: Evolution in Remote Sensing, pp. 1–4. https://doi.org/10.1109/WHISPERS.2009.5288972.

McClatchey, R.A., Fenn, R.W., Selby, J.E.A., Volz, F.E., Garing, J.S., 1971. Optical properties of the atmosphere AFCRL-71-0279. Environ. Res. Pap. 354, 108.

Mishra, M.K., Rathore, P.S., Misra, A., Kumar, R., 2020. Atmospheric Correction of Multispectral VNIR Remote Sensing Data: Algorithm and Inter-sensor Comparison of Aerosol and Surface Reflectance Products. Earth Space Sci. 7, e2019EA000710. https://doi.org/10.1029/2019EA000710.

Nascimento, J.M., Véstias, M.P., Martín, G., 2020. Hyperspectral compressive sensing with a system-on-chip FPGA. IEEE J. Sel. Top. Appl. Earth Obs. Remote Sens. 13, 3701–3710.

Nia, M.S., Wang, D.Z., Bohlman, S.A., Gader, P., Graves, S.J., Petrovic, M., 2015. Impact of atmospheric correction and image filtering on hyperspectral classification of tree species using support vector machine. J. Appl. Remote Sens. 9 (1), 095990. https://doi.org/10.1117/1.JRS.9.095990.

Qu, Y., Qi, H., Ayhan, B., Kwan, C., Kidd, R., 2017. DOES multispectral / hyperspectral pansharpening improve the performance of anomaly detection?, in: 2017 IEEE International Geoscience and Remote Sensing Symposium (IGARSS). Presented at the 2017 IEEE International Geoscience and Remote Sensing Symposium (IGARSS), pp. 6130–6133. https://doi.org/10.1109/IGARSS.2017.8128408.

Sabater, N., Vicent, J., Alonso, L., Cogliati, S., Verrelst, J., Moreno, J., 2017. Impact of Atmospheric Inversion Effects on Solar-Induced Chlorophyll Fluorescence: Exploitation of the Apparent Reflectance as a Quality Indicator. Remote Sens. 9, 622. https://doi.org/10.3390/rs9060622.

Seong, N.-H., Jung, D., Kim, J., Han, K.-S., 2020. Evaluation of NDVI Estimation Considering Atmospheric and BRDF Correction through Himawari-8/AHI. Asia-Pac. J. Atmospheric Sci. 56 (2), 265–274. https://doi.org/10.1007/s13143-019-00167-0.

Smith, G.M., Milton, E.J., 1999. The use of the empirical line method to calibrate remotely sensed data to reflectance. Int. J. Remote Sens. 20 (13), 2653–2662. https://doi.org/10.1080/014311699211994.

Sundberg, R., 2018. The Impact of Cloud Shadows on Subpixel Target Detection, in: 2018 9th Workshop on Hyperspectral Image and Signal Processing: Evolution in Remote Sensing (WHISPERS). IEEE, pp. 1–5.

Taghipour, A., Ghassemian, H., 2017. Hyperspectral Anomaly Detection Using Attribute Profiles. IEEE Geosci. Remote Sens. Lett. 14 (7), 1136–1140. https://doi.org/10.1109/LGRS.2017.2700329.

Tewkesbury, A.P., Comber, A.J., Tate, N.J., Lamb, A., Fisher, P.F., 2015. A critical synthesis of remotely sensed optical image change detection techniques. Remote Sens. Environ. 160, 1–14. https://doi.org/10.1016/j.rse.2015.01.006.

van der Meer, F., 2006. The effectiveness of spectral similarity measures for the analysis of hyperspectral imagery. Int. J. Appl. Earth Obs. Geoinform. 8 (1), 3–17. https://doi.org/10.1016/j.jag.2005.06.001.

Wang, T., Du, B., Zhang, L., 2013. A Kernel-Based Target-Constrained Interference-Minimized Filter for Hyperspectral Sub-Pixel Target Detection. IEEE J. Sel. Top. Appl. Earth Obs. Remote Sens. 6 (2), 626–637. https://doi.org/10.1109/JSTARS.2013.2251863.

Wang, Z., Xue, J.-H., 2017. The matched subspace detector with interaction effects. Pattern Recognit. 68, 24–37. https://doi.org/10.1016/j.patcog.2017.03.002.

Wilson, R.T., Milton, E.J., Nield, J.M., 2014. Spatial variability of the atmosphere over southern England, and its effect on scene-based atmospheric corrections. Int. J. Remote Sens. 35 (13), 5198–5218. https://doi.org/10.1080/01431161.2014.939781.

Xu, F., Liu, J., Sun, M., Zeng, D., Wang, X., 2017. A Hierarchical Maritime Target Detection Method for Optical Remote Sensing Imagery. Remote Sens. 9, 280. https://doi.org/10.3390/rs9030280.

Yadav, D., Arora, M.K., Tiwari, K.C., Ghosh, J.K., 2018. Parameters affecting target detection in VNIR and SWIR range. Egypt. J. Remote Sens. Space Sci. 21 (3), 325–333.

Yarbrough, A.W., Mendenhall, M.J., Martin, R.K., 2010. The effects of atmospheric mis-estimation on hyperspectral-based adaptive matched filter target detection as measured by the bhattacharyya coefficient, in: 2010 2nd Workshop on Hyperspectral Image and Signal Processing: Evolution in Remote Sensing. IEEE, pp. 1–4.

Yuen, P.WT., Richardson, M., 2010. An introduction to hyperspectral imaging and its application for security, surveillance and target acquisition. Imaging Sci. J. 58 (5), 241–253.

Zhang, L., Zhang, L., Tao, D., Huang, X., Du, B., 2014. Hyperspectral Remote Sensing Image Subpixel Target Detection Based on Supervised Metric Learning. IEEE Trans. Geosci. Remote Sens. 52, 4955–4965. https://doi.org/10.1109/TGRS.2013.2286195.